Icarus 386 (2022) 115114

Contents lists available at ScienceDirect

Icarus

journal homepage: www.elsevier.com/locate/icarus

Constraining the spectral behavior of the clay-bearing outcrops in Oxia Planum, the landing site for ExoMars "Rosalind Franklin" rover

Jeremy Brossier *, Francesca Altieri, Maria Cristina De Sanctis, Alessandro Frigeri, Marco Ferrari, Simone De Angelis, Andrea Apuzzo, Nicole Costa, Ma_MISS team

Institute for Space Astrophysics and Planetology IAPS, National Institute of Astrophysics, 100 Via del Fosso del Cavaliere, 00133 Rome, Italy

ARTICLE INFO

Keywords:
Mars
Oxia Planum
Landing site
Spectral analysis
Clay minerals
Carbonates

ABSTRACT

Oxia Planum (335.5°E, 18.2°N) is selected as the landing site for ExoMars rover mission (ESA/Roscosmos), where the "Rosalind Franklin" rover is scheduled to land in the decade. The region reveals several extensive clay-bearing outcrops recently exhumed, where biosignatures are possibly preserved. The objectives of the mission are to search for organics and investigate traces of past or extant life on Mars. Preliminary surveys of these outcrops show infrared absorptions typical of Fe,Mg-rich clays in the 1.0–2.6 μm range (1.4, 1.9, 2.3 and 2.4 μm) and an additional absorption at 2.5 μm implying a possible mixture with other mineral phase(s). Here we provide a detailed description of absorptions of the clay-rich materials detected in Oxia Planum, and map their strength and distribution throughout the region using hyperspectral data gathered by the Compact Reconnaissance Imaging Spectrometer for Mars (CRISM) onboard NASA's Mars Reconnaissance Orbiter (MRO) mission. Our analysis suggests that the Fe,Mg-rich clays identified in Oxia Planum mainly correspond to either Fe-bearing saponites (e.g., Griffithite) or vermiculite ores (i.e., vermiculite associated with a hydrobiotite component). Conversely, large clay-bearing outcrops found in the catchment area (337°E, 16.7°N) are rather consistent with nontronites in association with Al-rich clays and kaolins, in agreement with previous identification in the Mawrth Vallis – west Arabia Terra province. Presence of Fe,Ca-rich carbonates is recognized with the absorption near 2.53 μm and the observation of a broad peak in the 3–4 μm range, supporting their co-occurrence with the clays in Oxia Planum and its catchment area. Although we favor a pedogenesis alteration for the clays found in the catchment area, the origin of those studied in Oxia's basin remains enigmatic, where alternative scenarios could be either lacustrine and deltaic sedimentation, groundwater circulation, or even hydrothermal fluid circulation. Future in-situ measurements by "Rosalind Franklin" rover will indubitably provide new insights on the mineralogical diversity seen in the region and their origins.

1. Introduction

1.1. What do we know so far?

ExoMars rover mission (ESA/Roscosmos) is scheduled to launch in the following years and will deliver the "Rosalind Franklin" rover to explore Oxia Planum (335.5°E, 18.2°N), a region that straddles at the edge of Chryse Planitia basin (Fig. 1). Oxia Planum bears several morphological and mineralogical evidences of a long-lived aqueous activity, and also exposes sedimentary rocks where biosignatures might be preserved (e.g., Carter et al., 2016; Mandon et al., 2021; Quantin-Nataf et al., 2021). ExoMars landing ellipse is located on the northern part of a plain where widespread clay minerals have been identified (Fig. 1), at the outlet of the Coogoon Valles system (Molina et al., 2017; Fawdon et al., 2021a). Indeed, orbital data reveal extensive outcrops of ancient clay-rich rocks, thought to be recently exhumed (Carter et al., 2016). These rocks will be accessible to the rover and its nine instruments to search for signs of past or present life on Mars by investigating the surface and shallow subsurface at Oxia Planum (Vago et al., 2017).

Oxia's clay mineralogy seems homogeneous throughout the landing ellipse and its close surroundings (Carter et al., 2016; Mandon et al., 2021). A preliminary survey by Mandon et al. (2021) shows narrow absorptions centered at 1.4, 1.9 and around 2.3 μm and another, weaker absorption around 2.4 μm. Such absorptions are indicative of intermediate Fe,Mg-rich clays (e.g., vermiculite and Fe-rich saponite). They also report an additional, relatively shallow absorption around 2.5 μm, suggesting a possible mixture with carbonates or other phyllosilicates (e.

* Corresponding author.
E-mail address: jeremy.brossier@inaf.it (J. Brossier).

https://doi.org/10.1016/j.icarus.2022.115114
Received 25 January 2022; Received in revised form 24 May 2022; Accepted 26 May 2022
Available online 22 June 2022

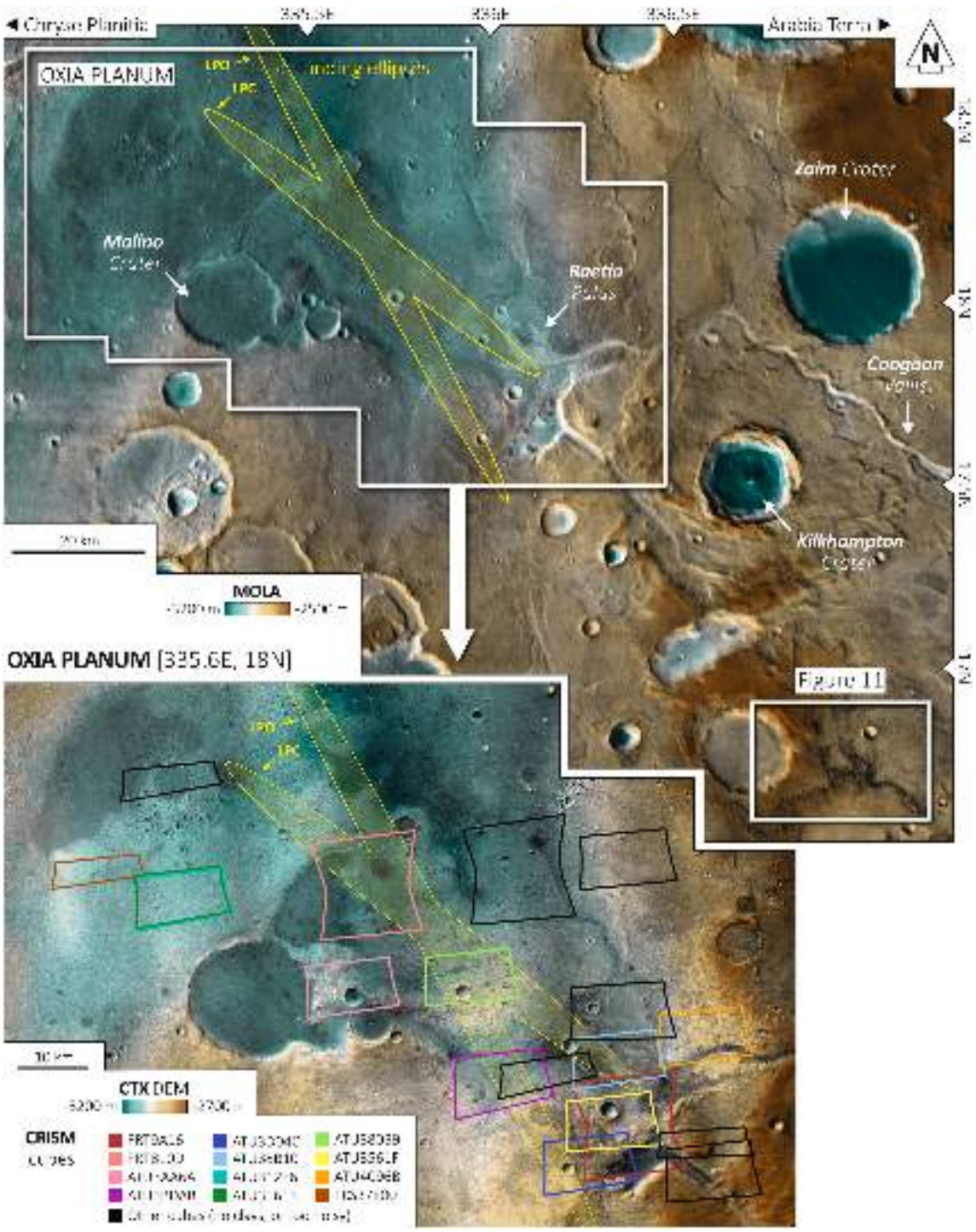

Fig. 1. (top) Oxia Planum through THEMIS infrared daytime map overlain by the color-shaded MOLA (lower elevations in teal and higher elevation areas in brown). The location of an isolated outcrop in the catchment area of Coogoon Valles is also indicated (Fig. 11). (bottom) Closer view on the landing site (335.6°E, 18°N) through CTX mosaic overlain by the color-shaded CTX DEM. Color-coded footprints correspond to CRISM cubes used in this work. Black footprints display other cubes that are not selected for further analysis since no clay-bearing outcrops have been clearly detected therein. Yellow ellipses indicate the opening (LPO) and closing (LPC) of the scheduled launch windows. (For interpretation of the references to color in this figure legend, the reader is referred to the web version of this article.)

g., serpentines or chlorites).

1.2. What needs to be done?

Hydrated minerals usually display two strong absorptions: one near 1.4 μm is due to structural OH and the second near 1.9 μm is due to the H_2O (interlayer water) stretching and bending modes. Phyllosilicates have typical absorptions within the 2.2–2.4 μm spectral range assigned to M-OH bonds (M being Al, Fe or Mg) (Hunt, 1977; Clark et al., 1990). Al-rich phyllosilicates (montmorillonite) display a characteristic absorption near 2.21 μm due to structural Al–OH bending and stretching modes. Al,Fe-rich phyllosilicates (nontronite) have absorptions at

Table 1
Main characteristics of the cubes targeting Oxia Planum used in our study (coordinates, collection date). Notes: (1) Two extra cubes covering outcrops in the catchment area (337°E, 16.7°N).

CRISM Cubes	Longitude (°E)	Latitude (°N)	Date
FRT810D	335.5	18.2	Oct. 2007
FRT9A16	336.1	17.7	Jan. 2008
ATU3AA6A	335.5	18.1	Feb. 2016
ATU3BDAB	335.8	17.8	May 2016
ATU3D04C	336	17.7	June 2016
ATU38B10	336.1	17.9	Oct. 2015
ATU312E6	335.1	18.3	July 2014
ATU356F3	335.1	18.3	Feb. 2015
ATU380B9	335.7	18.1	Sep. 2015
ATU3561F	336.1	17.8	Feb. 2015
ATU4096B	336.3	18	Dec. 2016
FRS37E00	334.9	18.4	Aug. 2015
FRT8438 (1)	336.94	16.8	Oct. 2007
FRT10FE9 (1)	337.04	16.8	Feb. 2009

2.28–2.29 μm and a weaker one at 2.40–2.41 μm due to AlFe-OH and Fe-OH combination bands. Diversely, Mg-rich phyllosilicates (saponite) have absorptions at 2.31–2.32 μm and a weaker one at 2.38–2.39 μm due to Mg-OH bending and stretching modes (e.g., Clark et al., 1990; Bishop et al., 2013a). Mixing of Fe-rich endmember and Mg-rich endmember leads to a shift in the absorption near 2.3 μm between 2.28 and 2.32 μm (also near 1.4 and 2.4 μm), depending on the Fe/Mg ratio (e.g., Michalski et al., 2015). Carbonates have typical absorptions in the 2.3–2.5 μm spectral region due to X-CO_3^{2-} vibrations (X being Mg, Fe or Ca) (Gaffey, 1987). More precisely, Mg-rich carbonates (magnesite) have paired absorptions at 2.30 and 2.50 μm, Fe-rich carbonates (siderite) at 2.33 and 2.53 μm, Ca-rich carbonates (calcite) at 2.34 and 2.54 μm (Gaffey, 1987; Hunt and Salisbury, 1971). As for phyllosilicates, positions of carbonate absorptions in this range depend on their composition (notably the mass of the major cation present therein). A detailed survey over the 1.0–2.6 μm spectral range is therefore mandatory to identify possible phyllosilicates and carbonates due to OH^- and CO_3^{2-} overtones.

Knowing the exact positions of the absorption band centers is crucial (1) to confirm (or infirm) possible mineral phase(s), and (2) to search for changes in clay mineralogies associated with differences in geochemical conditions, but also preservation or exhumation bias. Here we examine hyperspectral infrared data to investigate in detail the signatures of the clay outcrops and complement previous surveys (Fig. 1). We concentrate particularly on the absorptions centered at around 1.4, 2.3, 2.4 and 2.5 μm to better constrain the nature and composition of these outcrops, and to map their strength and distribution within Oxia's basin and its catchment area. Both approaches are done using the hyperspectral data collected by CRISM, the Compact Reconnaissance Imaging Spectrometer for Mars onboard NASA's MRO (Mars Reconnaissance Orbiter) mission.

1.3. Oxia Planum: landing site

Oxia Planum (18.2°N, 335.5°E) straddles the Martian crustal dichotomy between Ares Vallis and Mawrth Vallis, two major outflow channel systems. This region preserves ancient environments with clay minerals possibly older than 3.8 Ga, mid-Noachian or earlier (Tanaka et al., 2014; Quantin-Nataf et al., 2021). This extensive clay-bearing sedimentary formation is overlain by the vestiges of a past fluvio-deltaic lacustrine activity (Molina et al., 2017), possibly early Hesperian or older in age (Ivanov et al., 2020; Quantin-Nataf et al., 2021). A long-lived aqueous activity is evidenced by the presence of fluvio-deltaic features, including fan delta deposits (i.e., *Raetia Palus*), shallow riverbeds (e.g., *Aegyptus Vallis*) and sinuous ridges inferred as inverted channels at the outlet of the Coogoon Valles system (Molina et al., 2017). During the early Amazonian age, the region has been capped by a dark, rugged and massive formation (namely "dark resistant unit"), filling local topographic lows such as impact craters and ancient riverbeds (Quantin-Nataf et al., 2021). Since then, the area is under continuous long-term wind erosion, and the relatively "fresh" clay-bearing outcrops are accessible where the overlying materials have been recently eroded away. Crater obliteration rate implies that around 250 m of relief have been erased over the last 3 Ga (Quantin-Nataf et al., 2019, 2021). Presence of degraded ejecta and scattered rounded buttes (also "mounds" in McNeil et al., 2021), as well as many inverted morphologies (impact craters, channels) in Oxia Planum testifies the significant erosion occurring therein.

2. Data & methods

2.1. Spectral analysis

Spectral signatures of the clay-bearing outcrops are examined with data collected by CRISM instrument in targeted mode (Murchie et al., 2007, 2009). CRISM targeted data consist of spectral cubes at spatial resolutions of around 20–40 m per pixel and a spectral resolution of 6.6 nm. We focus on data acquired in the near-infrared spectral range between 1.0 and 4.0 μm, as it contains absorptions that help to identify hydrated minerals on Mars, notably from 1.3 to 2.6 μm (e.g., Bibring et al., 2005; Ehlmann et al., 2009; Carter et al., 2013). We have selected several CRISM data targeting Oxia Planum for this investigation (Fig. 1): two Full Resolution Targeted (FRT) cubes, nine Along-Track Undersampled (ATU) cubes and one Full Resolution Short (FRS) cube. We also included two FRT cubes targeting hydrated minerals in Oxia's catchment area (337°E, 16.7°N), for comparison purposes. Table 1 lists the main characteristics of the 14 cubes (center longitude and latitude, and collection date for each cube). Most of the cubes used in this work (i.e., FRS and ATU cubes) were acquired quite recently (2014–2016) and hence are noisier due to the aging of the instrument and the failing of a cryo-cooler (e.g., Parente et al., 2010; Bultel et al., 2015a). Only the FRT cubes were obtained during the nominal phase of the Mars Reconnaissance Orbiter mission (2007–2008). Since 2018, the infrared detector has been retired and no high-resolution data are being acquired in the near-infrared range.

CRISM cubes were first downloaded from the NASA Planetary Data System (PDS) server and then pre-processed through ENVI (version 5.4) which implements the CRISM Analysis Toolkit (CAT, version 7.4), a complementary tool developed by the CRISM team (Murchie et al., 2007; Pelkey et al., 2007). The tool pipeline includes (1) a calibration into reflectance (I/F), (2) an improved "volcano scan" atmospheric correction (McGuire et al., 2009; Morgan et al., 2011), and (3) a basic photometric correction. After correcting the cubes with CAT ENVI, we processed them in IDL (version 8.6), where we calculate a column-by-column ratio, with the featureless median spectrum of the column as the denominator. We also verify that pixels used for the median spectrum can be considered as neutral (featureless), and do not contain any spectral features characteristic of hydrated and/or mafic minerals. This procedure helps to reduce noise and residual atmospheric contributions, and finally, emphasize mineralogical absorptions in the ratioed spectrum (e.g., Bultel et al., 2015a).

We select our regions of interest (ROIs) in each ratioed cube, as the regions where the clays are predominant. We calculate the two band depths at 1.9 and 2.3 μm (e.g., Viviano-Beck et al., 2014) on the entire cube to automatically select the pixels with strong paired absorptions (over 1–5% and 0.5–3% for the absorptions at 1.9 and 2.3 μm, respectively, see Table S1.1). This allows us to consequently define the ROIs containing the largest amount of clays for each cube, as shown with FRT810D and FRT9A16 cubes in Oxia Planum as well as FRT8438 cube in the catchment area (Fig. 2). We also use an index map that combines the absorptions at 1.41 μm, 1.92 μm, 2.30 μm and 2.40 μm (Loizeau et al., 2018; Mandon et al., 2021), particularly useful to outline the clay-bearing outcrops. Fig. 2 denotes the good correlation between the index and our selected ROIs. All cubes that were processed and analyzed in our

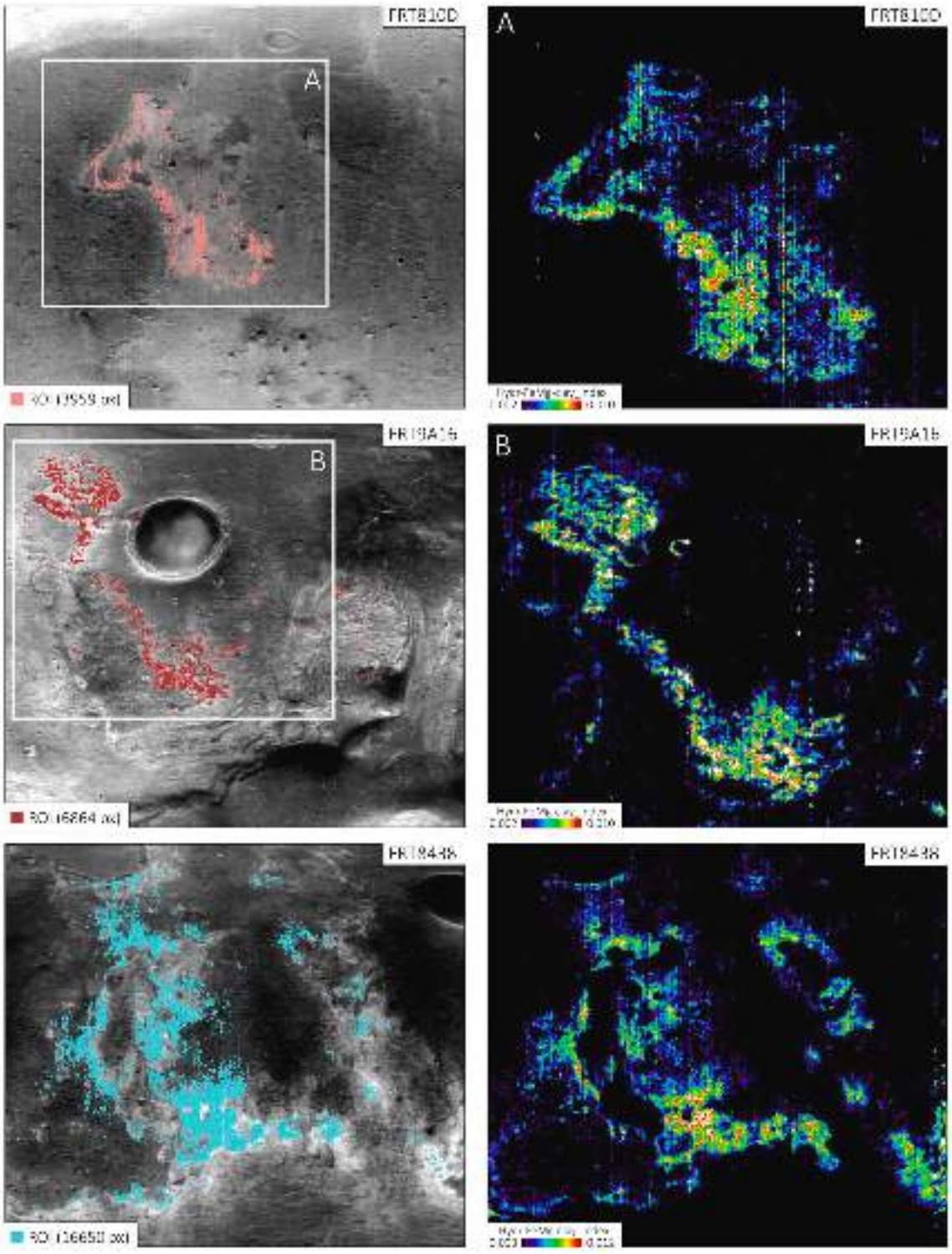

Fig. 2. Maps of the clay-bearing outcrops for (unprojected) cubes FRT810D (335.5°E, 18.2°N) and FRT9A16 (336.1°E, 17.7°N) targeting Oxia Planum, and FRT8438 (336.9.5°E, 16.8°N) in the catchment area. (left) Regions of interest (ROIs) are automatically determined for all pixels with strong absorptions at 1.9 and 2.3 μm (Viviano-Beck et al., 2014), and overlapping CRISM band at 1.30 μm. (right) Maps displaying the spectral criterion "Hydr-FeMg-clay index" adapted from Loizeau et al. (2018), combining the Fe,Mg-rich clay absorptions (1.41, 1.92, 2.30 and 2.40 μm).

study are shown in the supplementary materials 1 (Fig. S1.1).

All CRISM spectra shown and discussed in the present paper are acquired by averaging the pixels of the entire ROIs (number of pixels reported in Table 2), rather than smaller pixel regions. Smaller pixel regions are generally used to reduce the averaging over multiple surface materials. Nonetheless, clays in Oxia are assumed to be relatively homogeneous (Carter et al., 2016; Mandon et al., 2021; our study), and we are therefore not expecting small scale variations of different surface materials in our selected outcrops. Unlike Oxia Planum, smaller ROIs are highly required for similar analyses over Mawrth Vallis where a stronger mineralogical diversity is observed, with different mineral phases detected next to each other (e.g., Bishop et al., 2008a; McKeown et al., 2009).

Table 2
Band centers in the windows centered at 1.4, 2.3, 2.4 and 2.5 μm. Notes: (1) Spectral ranges that defined the windows of interest, and the tie points for continuum removal. (2) Number of pixels selected in the regions of interest (ROIs).

CRISM Cubes	1.4 μm (1.37–1.45 μm) [1]	2.3 μm (2.26–2.34 μm)	2.4 μm (2.36–2.44 μm)	2.5 μm (2.49–2.57 μm)	Pixels [2]
FRT810D	1.412 ± 0.008	2.306 ± 0.006	2.395 ± 0.007	2.531 ± 0.008	3959
FRT9A16	1.409 ± 0.008	2.308 ± 0.007	2.396 ± 0.008	2.530 ± 0.009	6864
ATU3AA6A	1.409 ± 0.008	2.305 ± 0.008	2.397 ± 0.009	2.530 ± 0.009	3538
ATU3BDAB	1.409 ± 0.010	2.304 ± 0.009	2.397 ± 0.009	2.530 ± 0.009	873
ATU3D04C	1.409 ± 0.009	2.306 ± 0.007	2.397 ± 0.009	2.528 ± 0.009	2424
ATU38B10	1.411 ± 0.010	2.303 ± 0.009	2.396 ± 0.009	2.528 ± 0.010	393
ATU312E6	1.408 ± 0.008	2.304 ± 0.008	2.398 ± 0.009	2.530 ± 0.009	7447
ATU356F3	1.408 ± 0.007	2.305 ± 0.008	2.396 ± 0.009	2.529 ± 0.009	13,038
ATU380B9	1.409 ± 0.008	2.309 ± 0.007	2.397 ± 0.009	2.530 ± 0.009	8601
ATU3561F	1.409 ± 0.009	2.307 ± 0.008	2.396 ± 0.009	2.531 ± 0.009	2030
ATU4096B	1.408 ± 0.008	2.303 ± 0.008	2.396 ± 0.009	2.530 ± 0.009	3749
FRS37E00	1.410 ± 0.008	2.304 ± 0.008	2.396 ± 0.009	2.530 ± 0.009	791
FRT8438	1.413 ± 0.008	2.296 ± 0.006	2.397 ± 0.008	2.530 ± 0.009	16,650
FRT10FE9	1.410 ± 0.009	2.297 ± 0.007	2.397 ± 0.008	2.530 ± 0.009	7305

2.2. GIS analysis

All imagery and topography datasets used in this study are available through the NASA Planetary Data System (PDS) server and integrated in a Geographic Information System (GIS) software (QGIS, version 3.18.3).

Our basemap (Fig. 1) is a mosaic of images collected by the ConteXT imager (CTX) at 6 m per pixel (Malin et al., 2007) that provides a geomorphological context for the clay-bearing outcrops detected in CRISM cubes. CTX-scale mapping identifies the spatial distribution of the diverse geologic features in Oxia Planum at regional scale (e.g., Ivanov et al., 2020; Quantin-Nataf et al., 2021; Fawdon et al., 2021b). Additionally, a mosaic of digital elevation models (DEMs) derived from CTX imagery offers the regional topography at a spatial resolution of about 10 m per pixel (Mandon et al., 2021; Quantin-Nataf et al., 2021). Both mosaics are produced for the ExoMars rover mission and are accessible from Fawdon et al. (2021b).

Detailed morphology and topography is captured by the High Resolution Imaging Science Experiment (HiRISE) (McEwen et al., 2007, 2010). HiRISE samples the Martian surface at very high spatial resolution (25–50 cm per pixel) and within three spectral wavelengths: blue-green (0.40–0.58 μm), red (0.57–0.83 μm) and near-infrared (0.79–1.10 μm) channels. In this study, we have integrated several HiRISE ("RED" and "COLOR") products over Oxia Planum (see Figs. S2.1–S2.2 and Table S2.1 in supplementary materials 2). RED products are full grayscale images (5–6 km wide) collected through the red filter, while COLOR products are three-color images (0.9–1.2 km wide) compiled from overlapping blue-green, red and near-infrared detectors. Digital terrain models (DTMs) are produced and released by the HiRISE team. They are derived from HiRISE stereo pairs (Kirk et al., 2009), where the two observations are acquired at the same ground location under different viewing angles. To date, 8 HiRISE DTMs intersecting the ExoMars landing ellipse are available and have been integrated in our GIS (see Fig. S2.3 and Table S2.2 in supplementary materials 2). Each HiRISE data is co-registered over the CTX mosaic with hundreds of manual tie points.

We divide this investigation by combining two complementary approaches: (1) survey on the infrared data to better describe the spectral signatures of the clay-bearing outcrops (Section 3.1) and (2) geological mapping to better understand the context of the outcrops (Section 3.2). We try to gather more details on the spectral data and complement recent analyses (Mandon et al., 2021; Quantin-Nataf et al., 2021).

3. Results

3.1. Spectral analysis

All CRISM spectra have been oversampled with a cubic spline interpolation, an IDL function. This spline function is applied on each pixel of a ROI in order to (1) create a fit that reproduces its spectrum, and (2) subsequently retrieve the absorption band center in each window of interest. We retrieve the values for each pixel of the ROIs within the four spectral ranges centered at 1.4, 2.3, 2.4 and 2.5 μm, after continuum removal to emphasize the absorptions (see tie points in Table 2). We first focus on the 2.3 μm window as it is the most discussed in the literature, unlike the others. Here, we do not analyze the 1.9 μm window (i.e., band center and shape) as it contains an instrumental artifact occurring often at 1.9 and 2.1 μm, resulting from the atmospheric removal pipeline (Leask et al., 2018). Figs. 3 to 5 illustrate the results obtained for FRT810D (335.5°E, 18.2°N) near the landing ellipse center, FRT9A16 (336.1°E, 17.7°N) near the delta, and FRT8438 (336.9.5°E, 16.8°N) in the catchment area. Results for other cubes are given in the supplementary materials 1 (Figs. S1.2 to S1.5).

3.1.1. Oxia Planum

The histograms in Fig. 3 indicate the variation of the band center within a broad window centered at 2.3 μm (2.26 to 2.34 μm range). The band center does not strongly vary in the window, with values spanning from 2.298 to 2.314 μm (2.306 ± 0.008 μm). FRT810D cube (Fig. 3A) shows the average band center of 2.305 μm (i.e., average of the entire ROI), characteristic of Oxia's clays (Carter et al., 2016; Mandon et al., 2021). FRT9A16 cube shows an average band center at slightly higher wavelengths, above 2.311 μm (Fig. 3B). However, the band center histograms also show minor clusters at different wavelengths. The two outcrops in FRT810D and FRT9A16 cubes both present a small cluster of pixels with a band center near 2.298 μm that could be ascribed to possible changes in the clay mineralogy (see Section 4.1). The histograms of some other cubes (i.e., ATU3BDAB, ATU38B10 and FRS37E00) have a major cluster (large number of pixels) with typical band center below 2.30 μm, similar to the secondary clusters seen in FRT810D and FRT9A16 cubes (Fig. S1.2 in the supplementary materials 1).

The same procedure is used for the windows centered at 1.4 μm (1.37–1.45 μm), 2.4 μm (2.36–2.44 μm) and 2.5 μm (2.49–2.57 μm) (Fig. 4). Although these bands are often at noise level in CRISM data, they are commonly used to provide complementary information about the species producing such absorptions in the 1.0–2.6 μm spectral range (e.g., Bishop et al., 2008a; Ehlmann et al., 2009; Carter et al., 2013). In Oxia Planum, the band center at 1.4 μm spans between 1.402 and 1.416 μm (1.409 ± 0.007 μm). The two other absorptions at 2.4 and 2.5 μm are weaker relative to the narrow absorptions seen at 1.41, 1.92 and around 2.3 μm. In the 2.4 μm window, the band center varies between 2.388 and 2.406 μm (2.397 ± 0.009 μm), while it spans from 2.521 to 2.539 μm (2.530 ± 0.009 μm) in the 2.5 μm window.

3.1.2. Catchment area

The two extra cubes targeting large clay-bearing outcrops in the catchment area (i.e., FRT8438 and FRT10FE9) have slightly different

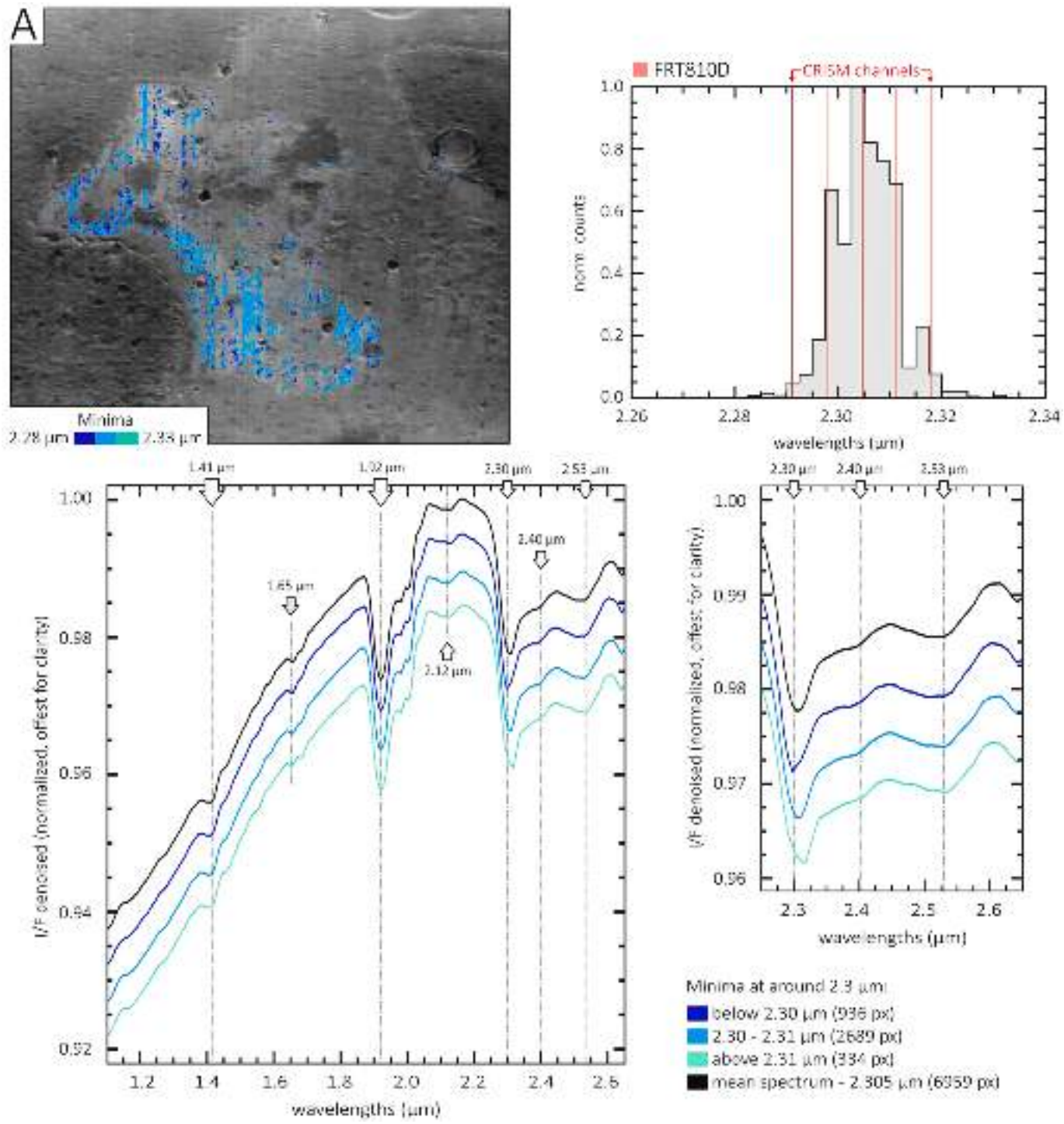

Fig. 3. (A) FRT810D cube near the landing ellipse center (335.5°E, 18.2°N): (top-left) Map displaying the distribution of the diverse band centers around 2.3 µm (2.26–2.34 µm) subdivided into 3 classes: (1) below 2.30 µm, (2) between 2.30 and 2.31 µm, and (3) above 2.31 µm. (top right) Histogram reporting the normalized counts (bins: 2.5 nm). Red vertical lines indicate the 5 CRISM spectral channels centered in the window. (bottom) Spectra of the CRISM denoised reflectance (normalized and offset for clarity) for the three classes and mean spectrum. White arrows indicate the main absorptions (1.41, 1.92, 2.30, 2.40 and 2.53 µm), while the gray arrow shows intermittent spikes associated with a detector filter at 1.65 µm. (B) Same for FRT9A16 cube near the delta (336.1°E, 17.7°N). (For interpretation of the references to color in this figure legend, the reader is referred to the web version of this article.)

values for the 1.4 and 2.3 µm windows (Table 2). Indeed, band centers in the 2.3 µm range tend to shorter wavelengths (2.296 ± 0.006 µm), while they display higher values in the 1.4 µm range (1.412 ± 0.008 µm) (Fig. 5A). Conversely, the band centers are rather similar in the 2.4 and 2.5 µm windows (2.397 ± 0.008 µm and 2.530 ± 0.009 µm, respectively) (Fig. 5B).

Table 2 reports the average band centers obtained on the ROIs within the four windows (centered at 1.4, 2.3, 2.4 and 2.5 µm) for all CRISM cubes.

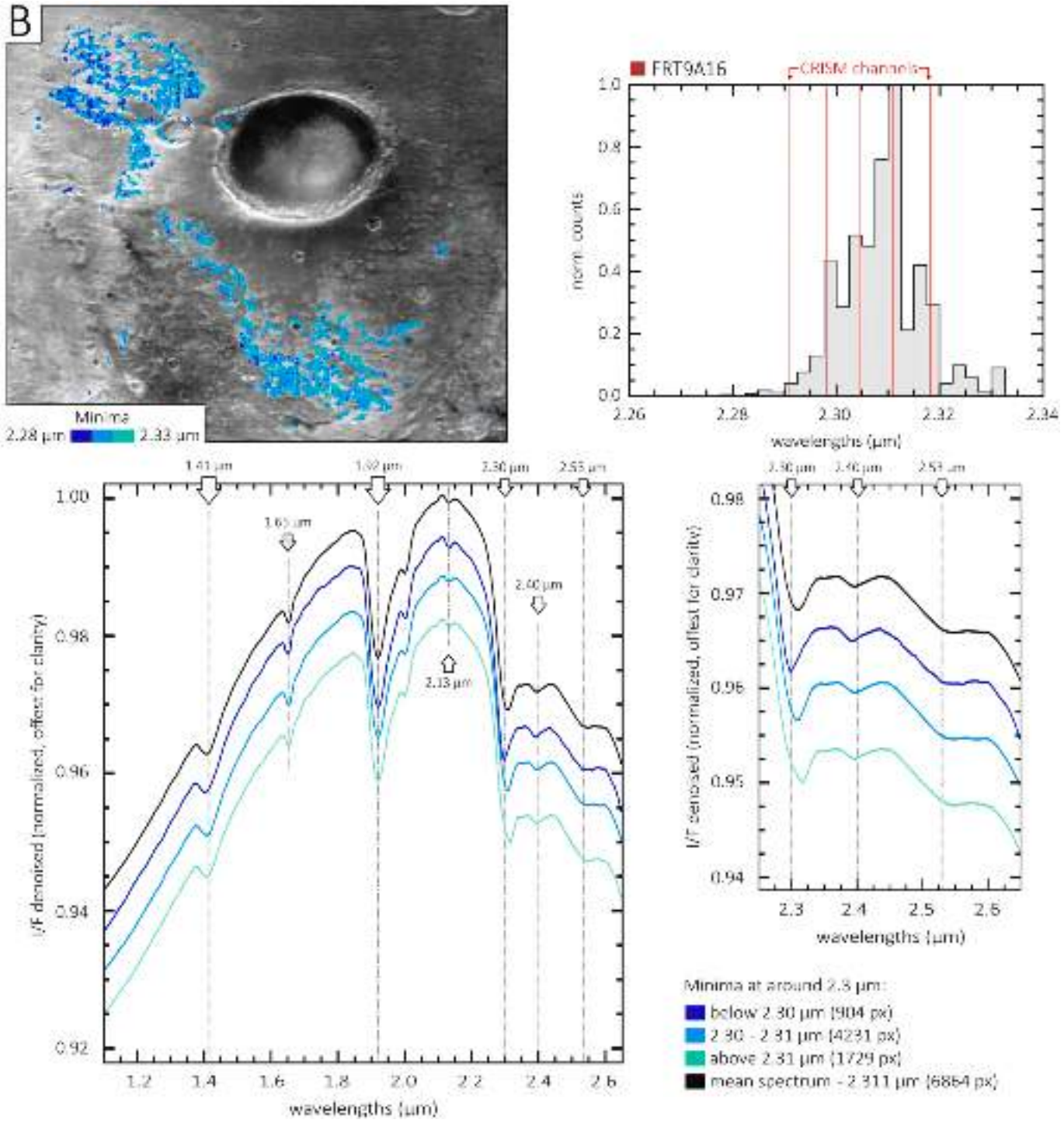

Fig. 3. (*continued*).

3.2. Geologic context

After the spectral survey, the CRISM cubes are projected and integrated into the GIS to map the clay-bearing outcrops and put them in context with the regional mapping (pink areas in Fig. 6). Geologic features were defined and mapped by a combination of albedo and topographic changes in the CTX data at regional scale and HiRISE data at local scale (e.g., Ivanov et al., 2020; Quantin-Nataf et al., 2021). Most features in Oxia Planum have been named after the provinces and towns of the Roman empire in 117 AD (Fawdon et al., 2021b). All units mapped in this study (i.e., clay outcrops and major geologic units) are made available as shapefiles in an online repository (Brossier et al., 2022).

We also mapped the extensive detection of hydrated phases from OMEGA ("Observatoire pour la Minéralogie, l'Eau, les Glaces et l'Activité") and CRISM multispectral data derived from Carter et al. (2016), for comparison purposes (light green in Fig. 6). This detection suggests a larger extent for the clay-bearing materials, although the datasets are significantly less resolved. Multispectral data from CRISM (MSP) have resolution of 100–200 m per pixel and a spectral sampling of around 56 nm (Murchie et al., 2007), while OMEGA data have lower resolutions of 350 m to 4 km per pixel and a spectral sampling of 13 nm

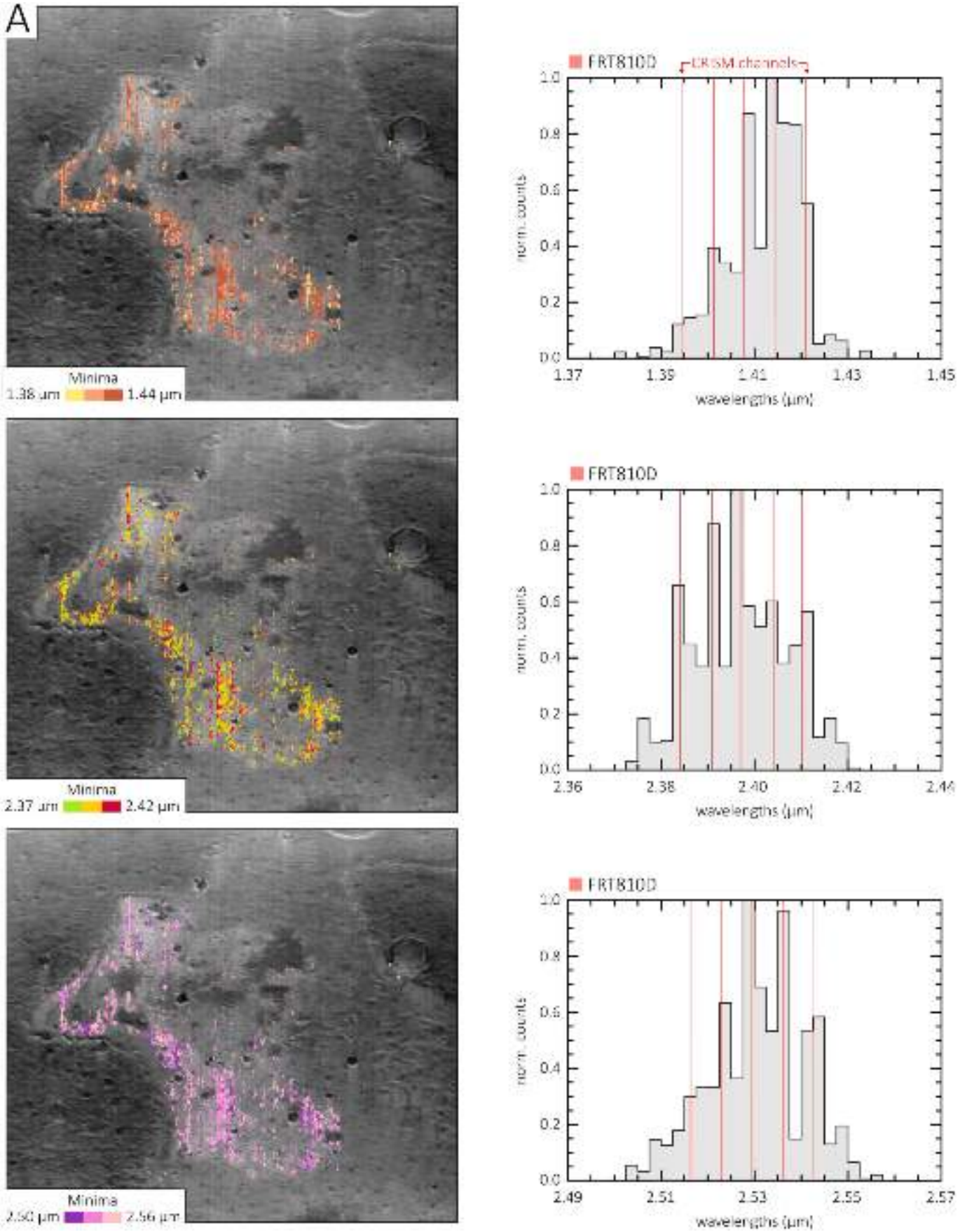

Fig. 4. (A) FRT810D cube near the landing ellipse center (335.5°E, 18.2°N): (left) Maps displaying the distribution of the diverse centers around 1.4 µm (1.37–1.45 µm), 2.4 µm (2.36–2.44 µm) and 2.5 µm (2.49–2.57 µm), which are subdivided into 3 classes. At 1.4 µm: (1) below 1.40 µm, (2) between 1.40 and 1.41 µm, and (3) above 1.41 µm. At 2.4 µm: (1) below 2.39 µm, (2) between 2.39 and 2.40 µm, and (3) above 2.40 µm. At 2.5 µm: (1) below 2.52 µm, (2) between 2.52 and 2.54 µm,

and (3) above 2.54 μm. (right) Histograms reporting the normalized counts (bins: 2.5 nm). Red vertical lines indicate the 5 CRISM spectral channels centered in the window. (B) Same for FRT9A16 cube near the delta (336.1°E, 17.7°N). (For interpretation of the references to color in this figure legend, the reader is referred to the web version of this article.)

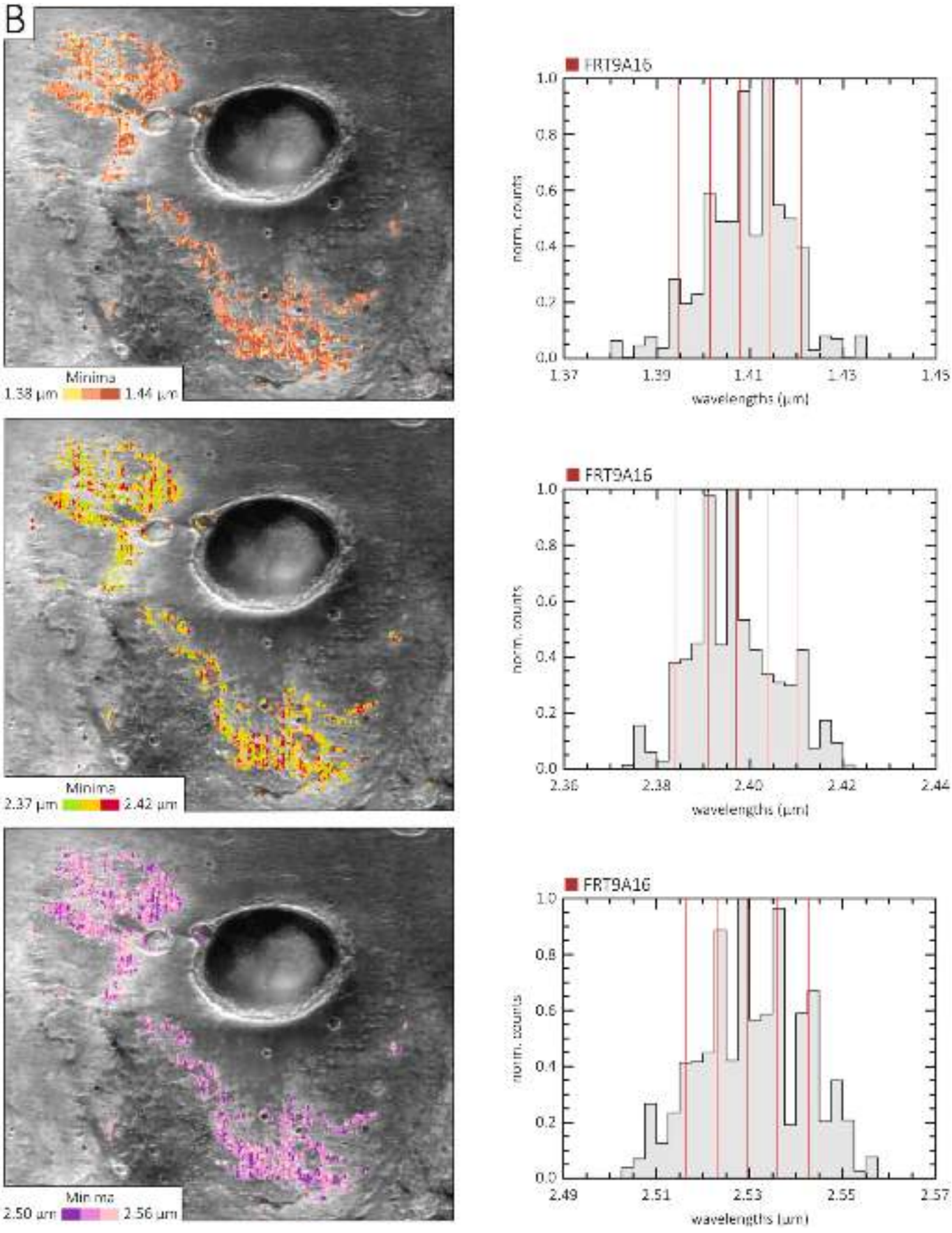

Fig. 4. (*continued*).

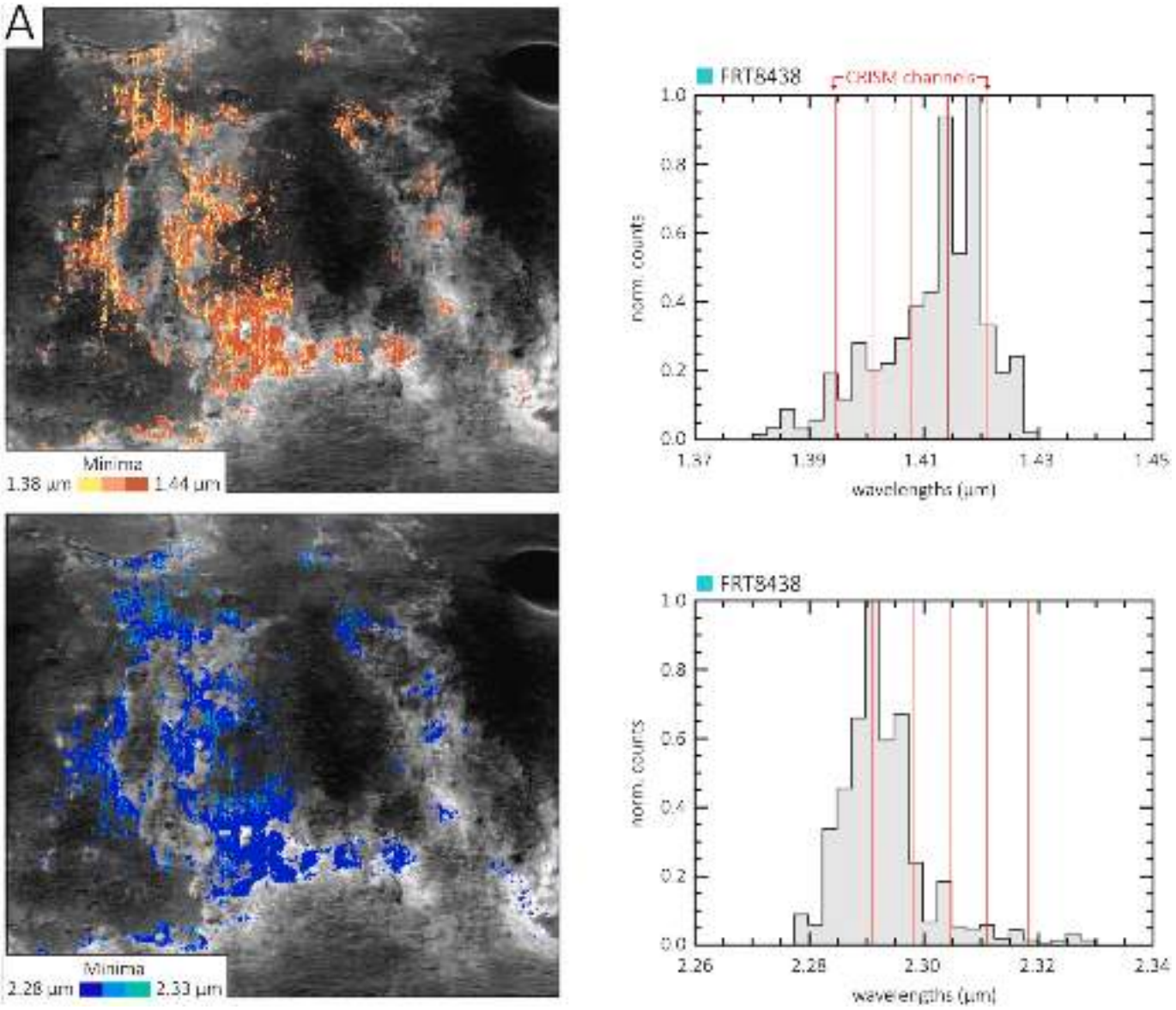

Fig. 5. FRT8438 cube in the catchment area (336.9.5°E, 16.8°N): Results obtained in the (A) 1.4 and 2.3 µm, and (B) 2.4 and 2.5 µm. Same annotations as in Figs. 3 and 4.

(Bibring et al., 2004, 2006).

The clay-bearing outcrops mapped in Fig. 6 appear as a fractured light-toned layer in high-resolution images (Quantin-Nataf et al., 2021; Mandon et al., 2021). Authors subdivided the clay-bearing formation into two subunits, based on their different aspects in the HiRISE color images (Delamere et al., 2010) and Colour and Stereo Surface Imaging System (CASSIS) (Thomas et al., 2017; Tornabene et al., 2017). The first unit has a yellow-orange tone (namely "orange" unit) with meter-sized fractures, while the second unit exhibits a rather bluer tone (namely "blue" unit) with decameter-sized fractures (Mandon et al., 2021; Parkes-Bowen et al., 2022). Outcrops mapped in our study (pink areas in Fig. 6) generally correspond to the orange unit and show the strongest clay absorptions; only the outcrop in the ATU38B10 cube corresponds to an area with a bluish appearance (Fig. 7C).

Altitudes for the mapped outcrops range from the highest areas at around −2790 m across the eastern plateaus to the deepest areas near −3150 m in Pannonia Planitia (Table 3). These values correlate well with the elevation range given in Quantin-Nataf et al. (2021) (−2600 to −3100 m) for the widespread clay detection derived from the multispectral data (Carter et al., 2016).

4. Discussion

4.1. Clay minerals

According to the spectral surveys over Oxia Planum, CRISM cubes reveal several absorptions within the near-infrared range from 1.0 to 2.6 µm (Carter et al., 2016; Mandon et al., 2021; this study), as shown in Fig. 8. Absorptions near 1.4 and 1.9 µm are common to all hydrated minerals, corresponding to a combination of H_2O bending and stretching modes (and OH vibrations near 1.4 µm). An absorption near 2.28–2.32 µm normally indicates a (Fe,Mg)-OH vibration, while an absorption near 2.16–2.21 µm implies an Al-OH vibration or Si-OH, depending on the shape of the absorption. These different absorptions and their shapes allow the distinction between the Fe,Mg-rich and Al-rich phyllosilicates (Hunt, 1977; Clark et al., 1990). Nontronites (Fe-rich clays) display typical absorption bands near 1.41–1.42 µm, 2.28–2.29 µm and 2.40–2.41 µm, while saponites (Mg-rich clays) have

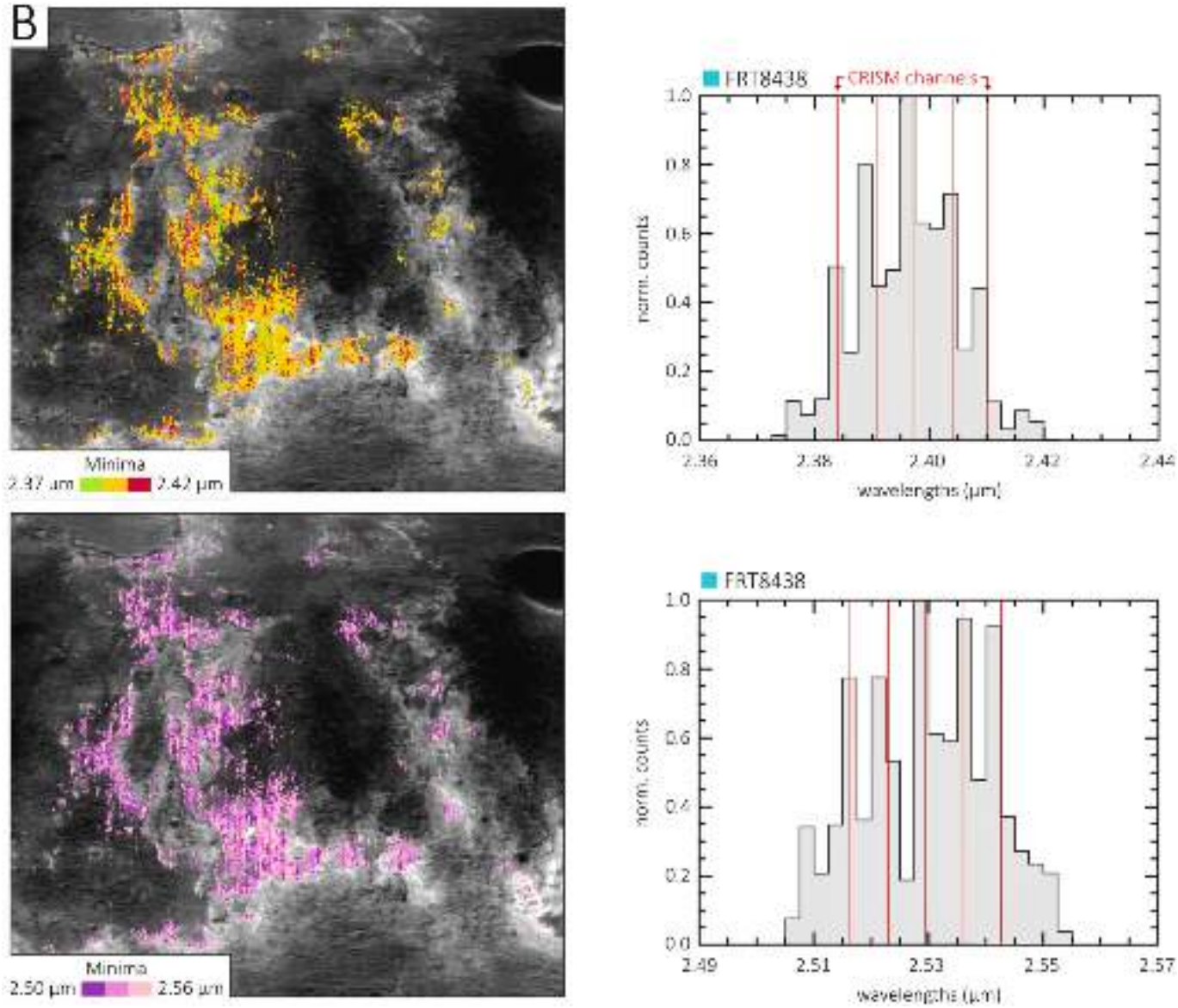

Fig. 5. (*continued*).

absorptions near 1.38–1.39 µm, 2.31–2.32 µm and 2.38–2.39 µm (Clark et al., 1990; Bishop et al., 2013a). Pure vermiculite (mica-type clay) shows typical band centers near 1.42, 2.30–2.31 µm and 2.39 µm (e.g., Carter et al., 2013; Swayze et al., 2018a). Fe-rich saponites (e.g., Griffith saponite or Griffithite) have characteristic absorptions near 1.40–1.42 µm, 2.30–3.32 µm and 2.40 µm (Treiman et al., 2014). Scatterplots of the terrestrial Fe,Mg-rich clays band centers in comparison with those derived in this study are reported in Fig. 9.

For comparison purposes, laboratory spectra of terrestrial analogues are shown in Fig. 10. They are obtained from the Reflectance Experiment Laboratory (RELAB) spectral repository (including spectra of analogous materials, e.g., Clark et al., 2007; Cloutis et al., 2007; Kokaly et al., 2017), which is regularly updated by the CRISM team through the CAT ENVI tool (e.g., Morgan et al., 2017). They demonstrate a good correspondence between CRISM data and the terrestrial clays (Figs. 8 and 9). It is worth noting that the RELAB spectrum of vermiculite generally used for reference in the literature (e.g, Carter et al., 2013; Mandon et al., 2021; Krzesińska et al., 2021) is actually "*not a match*" for vermiculite after verification through XRD diffraction measurements (sample labeled VER101, from University of Winnipeg, Cloutis, 2015). We therefore use another comparable, verified vermiculite spectrum from a different database: Libby GDS469L (Swayze et al., 2018b). This sample corresponds to handpicked ground flakes of vermiculite from a sample collected near Libby, Montana (Swayze et al., 2018a). We also add a reference spectrum for hydrobiotite (Libby GDS469M), which is often associated with vermiculite in vermiculite assemblages (or ores, as the term "ore" is generally used in geology for terrestrial mineral deposits). Hydrobiotite consists of mixed layers of vermiculite and biotite (Wilson, 1970; Brindley et al., 1983) and, like vermiculite, it results from the alteration of biotite or phlogopite (Velde, 1978). Its typical absorptions are slightly different: 1.40 µm, 2.32 µm and 2.38 µm (Swayze et al., 2018a). Considering this large variety of spectra for vermiculite ores, the range of values for band centers are broader than initially reported (e.g., Carter et al., 2013), as the vermiculite and hydrobiotite are commonly found together. Band centers may thus vary depending on the relative proportions of biotite (or phlogopite), hydrobiotite and vermiculite components in the mineral assemblages, according to the extent of vermiculization (Swayze et al., 2018a). Consequently, it is difficult to distinguish between the Fe-rich saponite and vermiculite ores since both share spectral similarities in the 1.0–2.6 µm range (Figs. 9 and 10), notably within the 1.4 and 2.3 µm windows.

Martian Fe,Mg-rich clays show spectral variability in the 1.4, 2.3 and

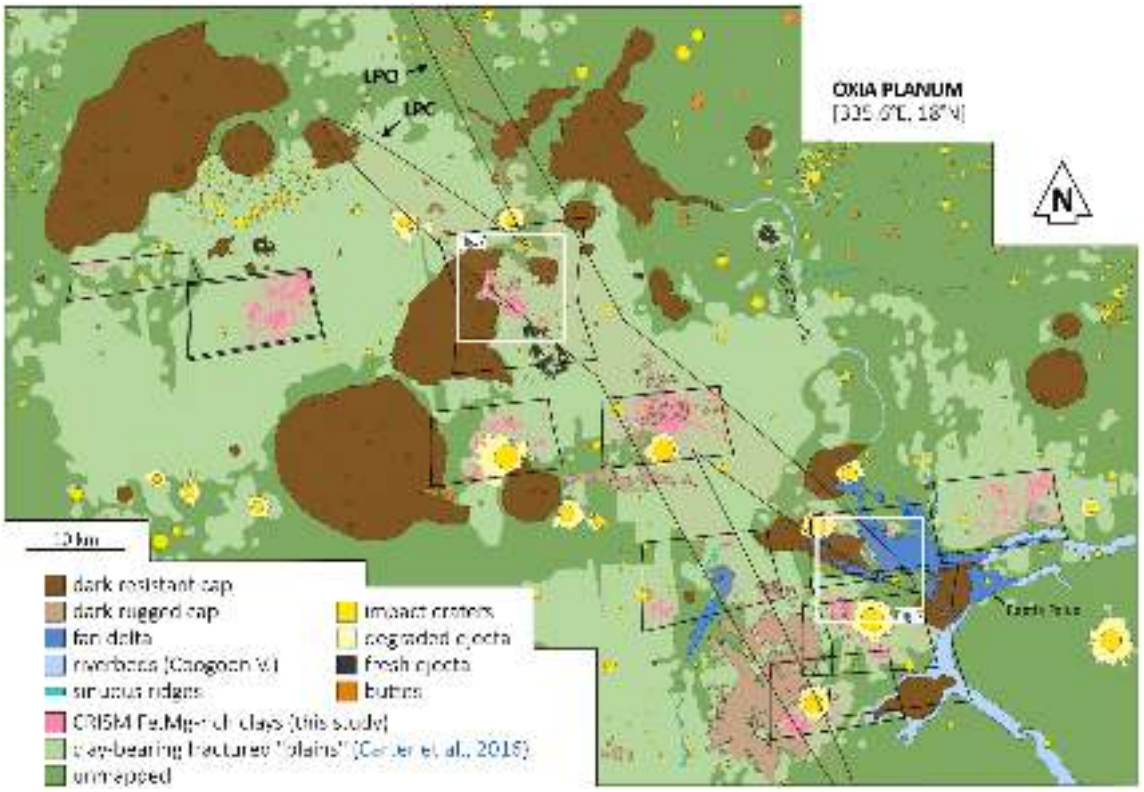

Fig. 6. Geologic map of Oxia Planum. Morphological units are defined from CTX imagery (Ivanov et al., 2020; Quantin-Nataf et al., 2021). Black footprints indicate the CRISM targeted data with the clay-bearing outcrops (in pink). White frames indicate the locations of two close-up views shown in Fig. 7. All units mapped here are provided as shapefiles though the online repository linked to this work (Brossier et al., 2022). (For interpretation of the references to color in this figure legend, the reader is referred to the web version of this article.)

2.4 μm absorptions, suggesting compositional changes from Fe-rich to Mg-rich endmembers (e.g., nontronite and saponite, respectively). Oxia's clays are consistent with Fe,Mg-rich clays, with combined absorptions at 1.41, 1.92, 2.30–2.31 μm and weaker overtones near 2.39–2.40 μm (Fig. 8). Fig. 9 summarizes the comparison between our observations and terrestrial clays, with band center ranges derived from the aforementioned literature. Band centers of 2.306 and 2.397 μm retrieved in Oxia Planum (Figs. 9 and 10) are rather consistent with Fe-rich saponites (smectitic clays) and vermiculite ores (mica-type clays) (Carter et al., 2016; Mandon et al., 2021). Presence of vermiculite is later discussed through recent mineralogical characterization of terrestrial analog rocks (Krzesińska et al., 2021). Moreover, vermiculite has been already suggested in mixtures with Fe-rich clays in the vicinity of Mawrth Vallis (e.g., Bishop et al., 2008a; McKeown et al., 2009) and other regions on Mars (e.g., Carter et al., 2013). Fe-rich saponites (e.g., Griffithite or Griffith saponite) are also good candidates regarding their intermediate band centers in the 1.4, 2.3 and 2.4 μm windows, as suggested for clays detected at Yellowknife Bay in Gale crater and elsewhere on Mars (Treiman et al., 2014). Conversely, Fe,Mg-rich clays found in Oxia's catchment area rather correspond to nontronite with a narrow absorption at 2.29 μm (Figs. 9 and 10) (also seen in Noe Dobrea et al., 2010). It would be conceivable to think that the clays studied in Oxia are a mixture of clay minerals derived from the catchment and those found in the basin (possible origin of the clays is discussed in Section 4.4). A mineral assemblage with mixed clays is consistent with detections made in the region immediately around Mawrth Vallis (e.g., Bishop et al., 2008a; McKeown et al., 2009; Noe Dobrea et al., 2010). Nonetheless, the band centers in Oxia's clays greatly match with the band positions of Fe-bearing saponites (Fig. 9, left) and vermiculite ores (with a hydrobiotite component) (Fig. 9, right), and further suggests that clays in the basin might correspond to one or the other, or even a mixture of the two phases.

Note however that the 1.4 μm window is also linked to a hydration absorption near 1.41 μm, in addition to the metal-OH overtone. This could explain the mismatch between the lab spectra and our data seen near 1.4 μm. Lab experiments on saponites (Treiman et al., 2014; Chemtob et al., 2015) show that desiccation strongly reduces the intensity of hydration absorptions at 1.4 and 1.9 μm. Authors also demonstrate that, under desiccating conditions, the band center near 1.4 μm is slightly shifted to lower wavelengths while the other absorptions at 2.3 and 2.4 μm remain unchanged. Thus, alone, the 1.4 μm absorption cannot provide a definitive selection among the different phases, but can be used in combination with other absorptions.

Considering the large variety of spectra for vermiculite ores (Swayze et al., 2018a, 2018b; Krzesińska et al., 2021), it seems that the 2.4-μm absorption is relatively stronger than in Fe-rich saponite (Treiman et al., 2014; Chemtob et al., 2015). Fe-rich saponite has a very weak overtone near 2.4 μm that only appears clearly when the continuum is removed (e.g., Treiman et al., 2014; Chemtob et al., 2015). Although being at noise level, this absorption is rather strong and clearly identified in Oxia's clays (Fig. 8), which could favor the presence of vermiculite. However, this sole characteristic does not allow us to discriminate between the vermiculite and Fe-saponite.

No Al-rich clays have been clearly detected in the CRISM cubes over Oxia Planum, although an absorption near 2.2 μm has been sporadically reported near the fan delta (associated with hydrated silica in Pan et al., 2021), and further east near Mawrth Vallis (e.g., McKeown et al., 2009; Noe Dobrea et al., 2010). Based on CRISM coverage, the closest detection is found within Oxia's catchment area (337°E, 16.7°N), and it suggests the presence of diverse clay mineralogies (e.g., Turner et al., 2021). FRT10FE9 and FRT8438 cubes cover an extensive light-toned deposit and their analysis shows co-occurrence of Al-rich clays and kaolins (green and cyan in Fig. 11), with a single absorption at 2.21 μm (e.g., montmorillonite, beidellite, illite) and a doublet absorption at 2.17

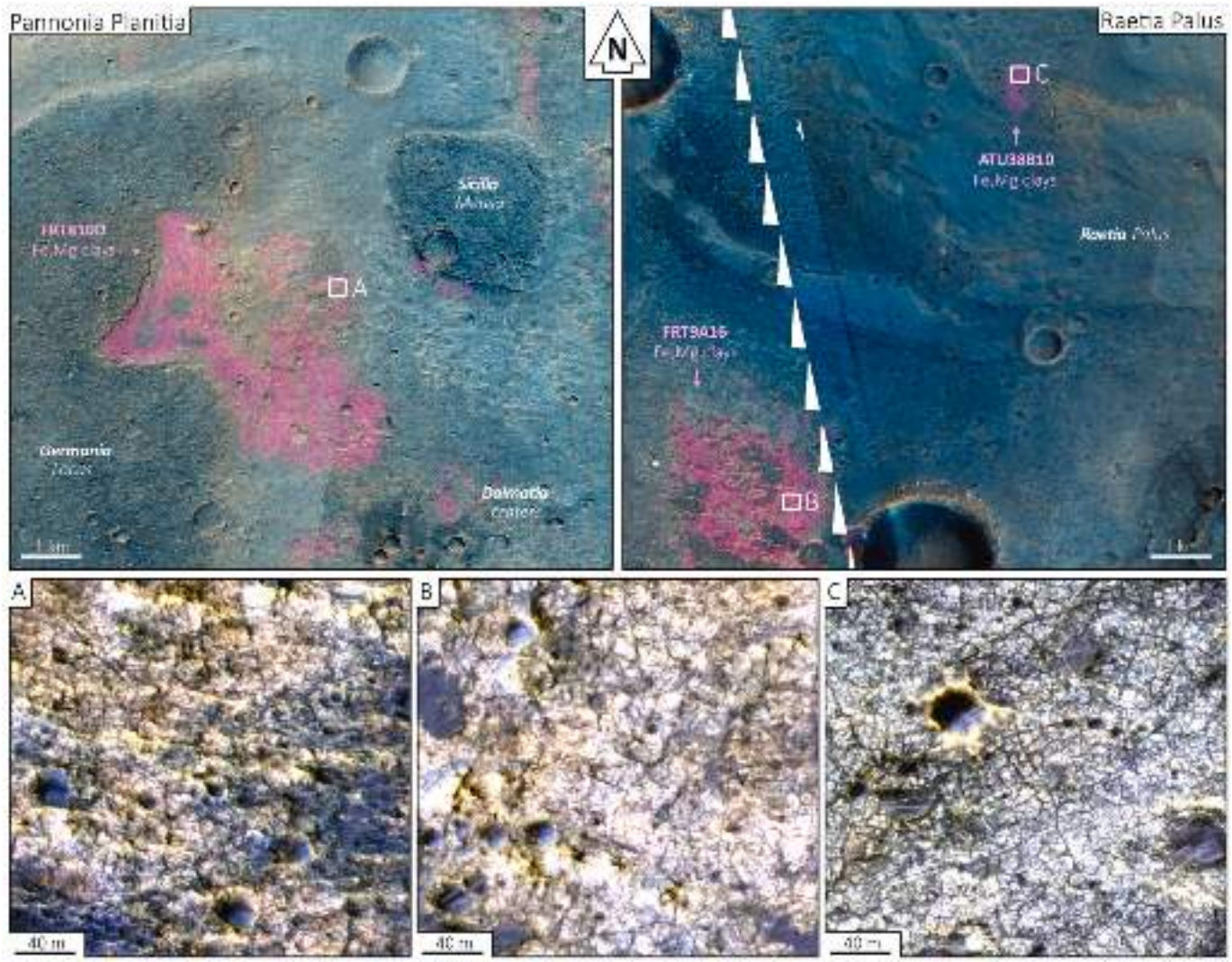

Fig. 7. Clay-bearing outcrops in (top left) Pannonia Planitia and (top right) Raetia Palus through CaSSIS color images (Fawdon et al., 2021b). Insets (A), (B) and (C) are close-up views with HiRISE color images to display their fractures and color variations. HiRISE images: (A) ESP_064828_1985, (B) ESP_063839_1980, and (C) ESP_060437_1980. Outcrops exhibit color variations: (A) FRT810D and (B) FRT9A16 have a yellow-orange tone, while (C) ATU38B10 shows a bluish tone. (For interpretation of the references to color in this figure legend, the reader is referred to the web version of this article.)

Table 3
Main characteristics of the clay-bearing outcrops mapped in Oxia Planum (surface areas and altitude ranges). Notes: (1) No values are reported for the cubes ATU356F3 and ATU3561F as they overlap with other cubes ATU312E6 and FRT9A16, respectively.

CRISM Cubes	Area (m^2)	Altitude Range (m)	Altitude (m)
FRT810D	7674	−3075 to −3146	−3118 ± 13
FRT9A16 (1)	7361	−2881 to −3009	−2939 ± 26
ATU3AA6A	6108	−2989 to −3112	−3053 ± 31
ATU3BDAB	4094	−2940 to −3048	−2986 ± 22
ATU3D04C	3994	−2883 to −2907	−2895 ± 5
ATU38B10	293	−3020 to −3030	−3027 ± 2
ATU312E6 (1)	14,898	−3053 to −3115	−3087 ± 12
ATU380B9	13,400	−2992 to −3075	−3042 ± 14
ATU4096B	11,297	−2787 to −3018	−2876 ± 41
FRS37E00	1251	−3009 to −3089	−3032 ± 15

and 2.21 μm (e.g., kaolinite, halloysite) (Noe Dobrea et al., 2010; Turner et al., 2021). These Al-rich clays lie on top of large exposures of Fe,Mg-rich clays with narrow absorption near 2.29 μm, typical of nontronites (purple in Fig. 11). This vertical sequence has been reported in previous studies in western Arabia Terra and Mawrth Vallis (e.g., Loizeau et al., 2010; Wray et al., 2008; McKeown et al., 2009; Loizeau et al., 2010; Noe Dobrea et al., 2010) and elsewhere on Mars (e.g., Ehlmann et al., 2009; Wray et al., 2009; Le Deit et al., 2012).

The positions of the absorption band centers at 1.4, 2.3 and 2.4 μm vary little throughout Oxia Planum. Exact positions of the band centers in these windows depend on the relative abundance of iron and magnesium in the clay structure, oxidation state of iron (e.g., Clark et al., 1990; Mustard, 1992; Chemtob et al., 2015; Michalski et al., 2015), as well as the proportions of specific clays possibly mixed in the outcrops.

4.2. Carbonates

In Oxia Planum, all twelve ROIs exhibit a broad, shallow absorption centered near 2.53 μm (Fig. 8). It appears in all the spectra showing strong absorptions near 1.9 and 2.3 μm, and is therefore detected over the "purest" clay-bearing outcrops. Generally, an increase in depth of the 2.5 μm band can be interpreted as indicative of the presence of carbonates and/or other phyllosilicates together with the Fe,Mg-rich clays, as suggested by Mandon et al. (2021).

Carbonates are frequently found near clays or mixed with them on Mars, like in Nili Fossae (Ehlmann et al., 2008a, 2009), Jezero crater (Ehlmann et al., 2008b; Horgan et al., 2020), Lybia Montes (Bishop

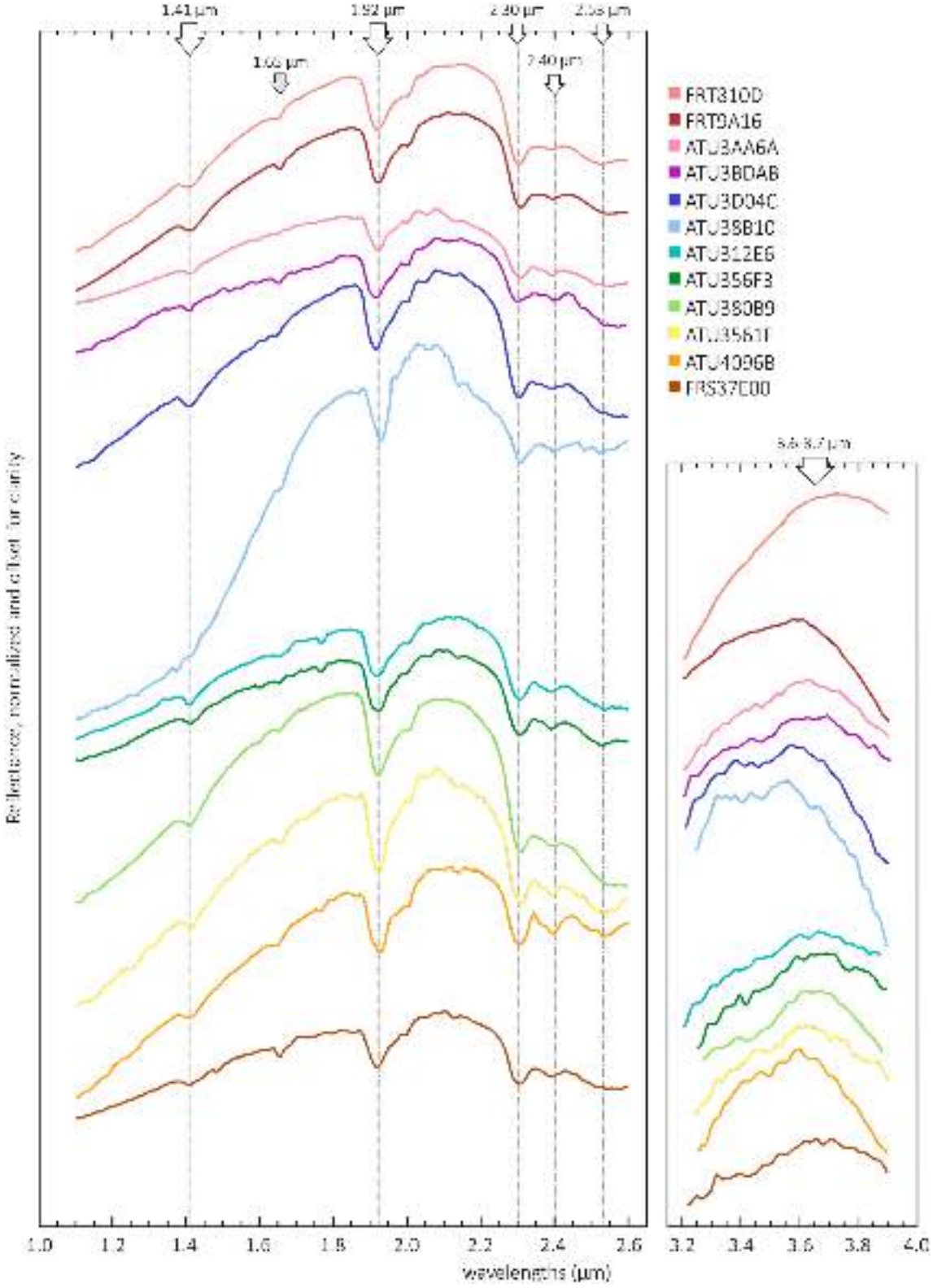

Fig. 8. Spectra of the CRISM denoised reflectance, normalized and offset for clarity. Unusable data at (1) 1.65 µm is associated with intermittent spikes from a detector filter boundary, (2) 2.60–2.80 µm is due to a saturated atmospheric CO_2 absorption there, and (3) 3.18 µm is an instrumental artifact (Murchie et al., 2007, 2009). Spectra are smoothed by averaging hundreds to thousands of pixels (Table 2). All spectra (notably ATU38B10) have a positive slope in the 1–2 µm range, likely due to the broad 1.2 µm absorption of a ferrous component (e.g., Bishop et al., 2008; McKeown et al., 2009). They all exhibit a broad "bulge-like" feature near 3.6–3.7 µm, typical of Martian carbonates (e.g., Bultel et al., 2019).

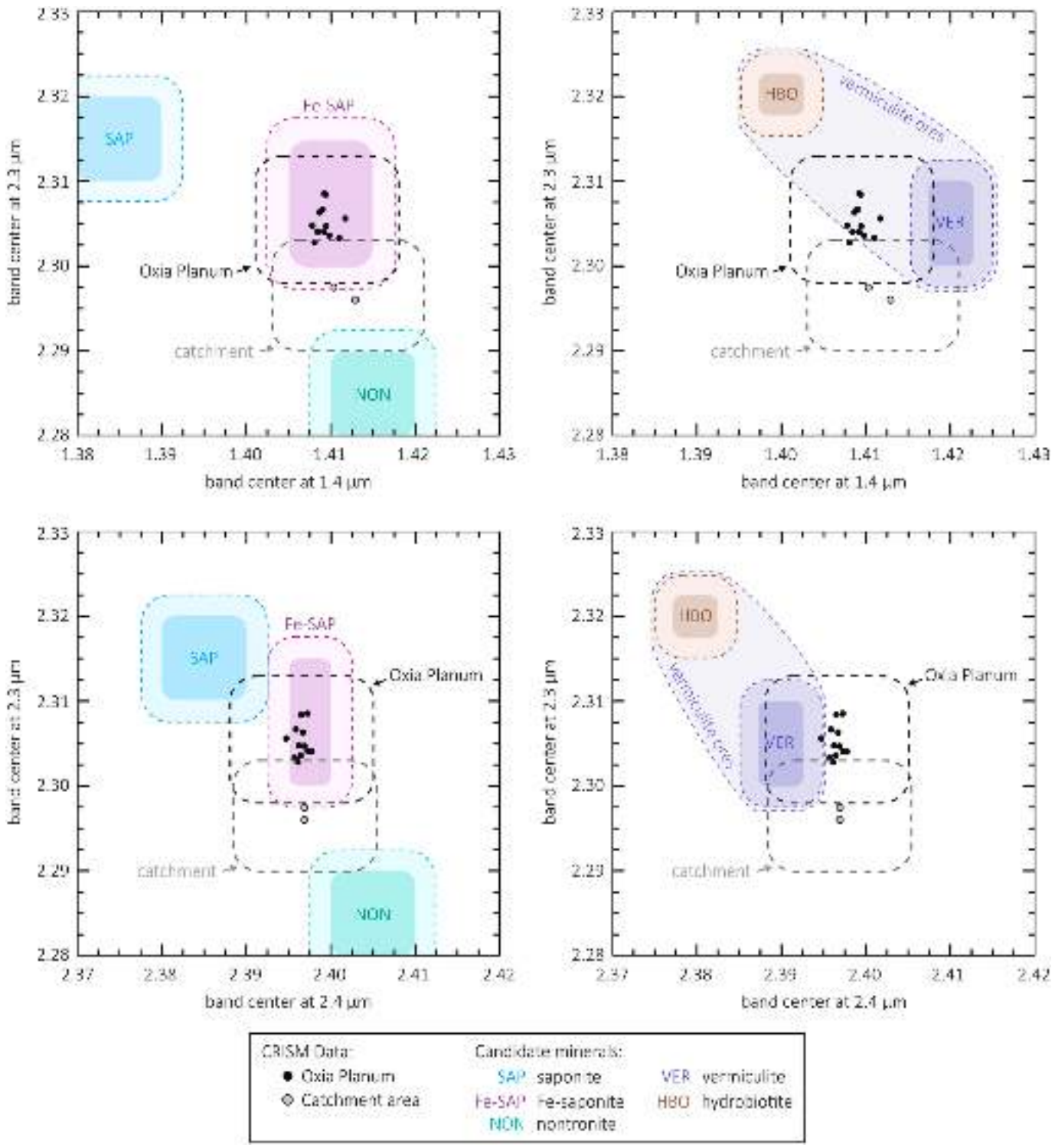

Fig. 9. (top) Scatterplots of 2.3 µm vs 1.4 µm band centers for the studied clay-bearing outcrops and candidate clays: nontronite and saponite (Clark et al., 1990; Bishop et al., 2013a), Fe-rich saponite (Treiman et al., 2014), and vermiculite ores (including pure vermiculite and hydrobiotite components separately) (Swayze et al., 2018a). (bottom) Scatterplots of 2.3 µm vs 2.4 µm band centers. Clay-bearing outcrops in Oxia display strong correlation with Fe-rich saponite (left panels) and also vermiculite ores (right panels), while outcrops identified in the catchment area are rather consistent with nontronites. Dashed outlines indicate the error areas: 2.5 nm for the candidate minerals (sampling) and standard deviations for the CRISM data analyzed here (Table 2).

et al., 2010; 2013a), Leighton crater (Michalski and Niles, 2010), McLaughin crater (Michalski et al., 2019), Mawrth Vallis (e.g., Bultel et al., 2019), Huygens crater (e.g., Wray et al., 2016), and Robert Sharp crater (Carter et al., 2015a; Brossier et al., 2021). They are usually best identified by paired absorptions at 2.3 and 2.5 µm in the 1.0–2.6 µm range, although the 2.3 µm range is strongly influenced by the presence of clays (e.g., Sutter et al., 2007; Bishop et al., 2013b). For instance, Bishop et al. (2013b) report that large amounts of carbonates are needed to shift the band center from 2.28–2.29 µm seen for Fe-rich clay (nontronite) toward 2.30–2.31 µm observed for Mg-rich carbonate

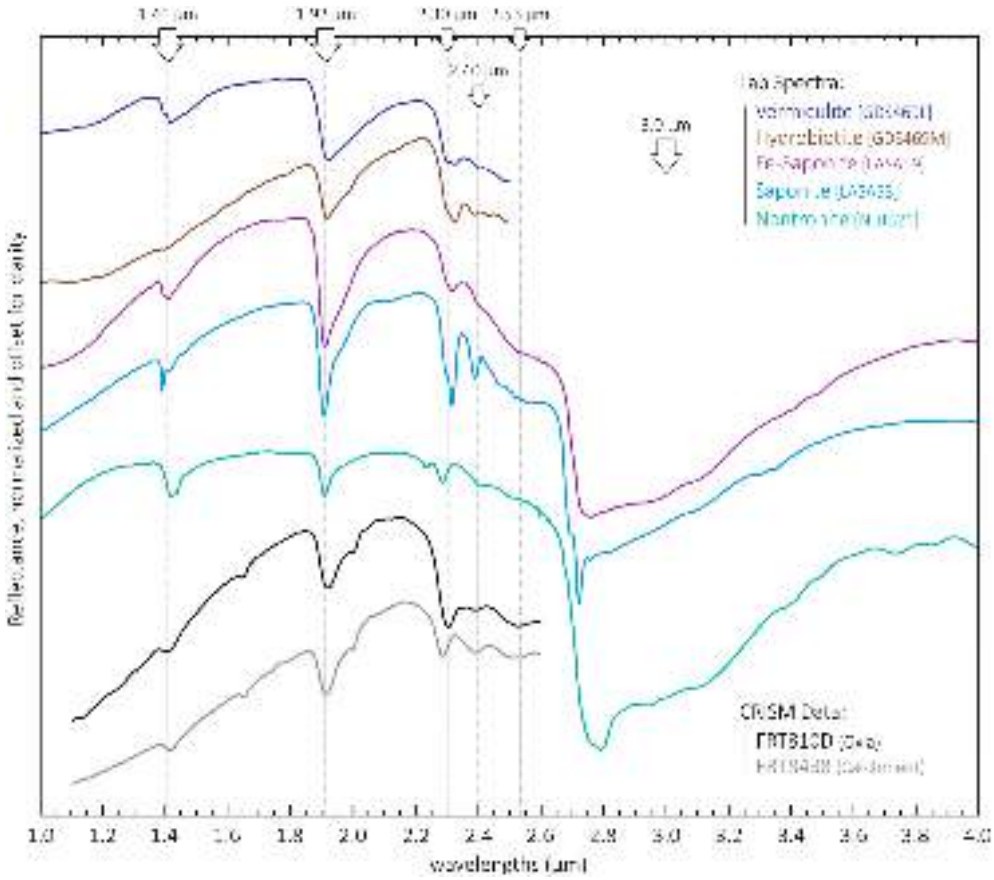

Fig. 10. Laboratory spectra of main candidate Fe,Mg-rich clays: nontronite, saponite, Fe-rich saponite (e.g., Griffithite) and vermiculite ore (vermiculite and hydrobiotite). All major absorptions are shown with vertical lines at 1.41, 1.92, 2.30, 2.40 and 2.53 µm.

(magnesite). The position of the 2.5 µm absorption in the carbonates spectra is indicative of the kind of cations present in the mineral structure (e.g., Mg, Fe or Ca). An absorption centered near 2.52–2.54 µm would be rather consistent with Fe,Ca-rich carbonates like siderites or calcites, whereas an absorption at shorter wavelengths is usually associated with Mg-rich carbonates like magnesites or even dolomites (Gaffey, 1986, 1987; Leask et al., 2021) (Figs. 12 and 13).

Fig. 12 summarizes the comparison between our observations and candidate carbonates, serpentines and chlorites, with band center ranges provided by the aforementioned literature. Laboratory spectra in Fig. 13 (RELAB spectral repository) show the additional absorptions that allow to discriminate the candidate minerals among the carbonates (3.4–3.5 µm and 3.8–3.9 µm), serpentines (2.10–2.12 µm) and chlorites (2.25–2.26 µm). Table 4 reports all band center values in the four windows of interest mentioned in this section (Section 4.1) for our observations and candidate mineral phases.

The presence of an absorption near 2.5 µm alone is not a sufficient criterion to identify carbonates. That is why, to complement this detection, we search for a specific pattern in the 3–4 µm range, where the presence of a broad peak near 3.6–3.7 µm is expected by deep absorptions near 3.4–3.5 µm and 3.8–3.9 µm (Fig. 8, right panel) due to carbonates. This feature is systematically attributed to carbonates (X-CO_3^{2-} vibrations), while other minerals commonly detected on Mars show a constant increase of reflectance in the 3.4–3.8 µm range (e.g., Gaffey, 1987; Hexter, 1958; Hunt and Salisbury, 1971; Hunt, 1977). Distinction between the various carbonate compositions could be determined with the band centers in the 3.4–3.5 µm range: Mg-rich (3.42 µm), and Fe,Ca-rich (3.45–3.50 µm) carbonates (Bultel et al., 2019). However, such a distinction cannot be assessed here due to the lack of a clear absorption near 3.4–3.5 in our observations (absent to weak). This is likely due to the deep water absorption near 3 µm induced by the clays that could subdue the carbonate absorption (Ehlmann et al., 2008a). Although the absorption at 3.8–3.9 µm cannot be entirely diagnosed due to the limited spectral range (CRISM IR: 1–4 µm), it can be retrieved through a drop of the spectrum near 3.9 µm. All the average CRISM spectra of the ROIs analyzed here show the expected "carbonates" feature in the 3–4 µm range (Fig. 8, right panel). We therefore calculate a spectral parameter ("BD3900") developed in Ehlmann et al. (2008a) to highlight the feature characteristic of carbonates and support their co-occurrence within the clay-bearing outcrops in Oxia Planum (Fig. 14). In the scatterplot (Fig. 14D), the BD3900 parameter correlates well with the Fe,Mg-rich clays index, showing high values in correlation with the clay exposures. Interestingly, carbonates have been previously reported in the catchment area along with the Mawrth Vallis area (Bultel et al., 2019) where they are collocated with the different clay minerals (i.e., nontronites, montmorillonites and kaolinites), indicating that carbonates may be present within Oxia's basin and its catchment. Present results (Fig. 14) indicate the presence of carbonates all over Oxia's clay-bearing outcrops targeted by CRISM data, and not only locally as suggested in the previous survey (Mandon et al., 2021).

Note that the 3–4 µm range is difficult to interpret, as it lacks a correction for the thermal emission contributions that reduce band strength (Blaney and McCord, 1989; Wagner and Schade, 1996). Additionally, this range suffers from a low signal-to-noise ratio of the detector (i.e., four times lower than the 1.0–2.6 µm spectral range), and an instrumental artifact at 3.18 µm that could obscure the 3.4–3.5 µm carbonate absorption (Murchie et al., 2009). Although a definitive identification and characterization of the carbonates is difficult owing to these issues, we remain confident in our observation considering the combined spectral features (i.e., an absorption near 2.53 µm together

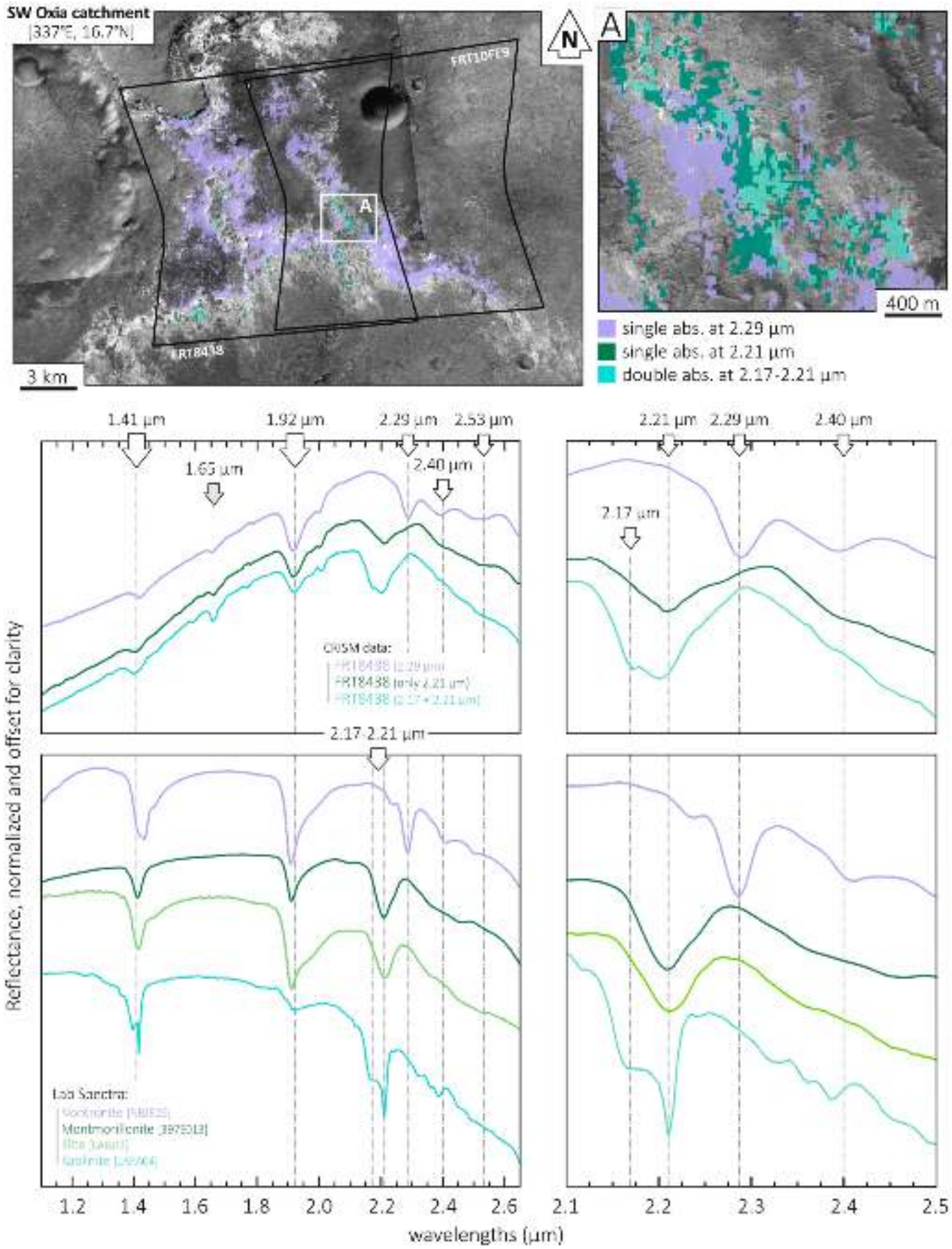

(caption on next page)

Fig. 11. Clay-bearing outcrops located in the catchment area of Oxia Planum (337°E, 16.7°N) with two CRISM cubes (FRT8438 and FRT10FE9). Different mineral phases are mapped using the parameters defined in Viviano-Beck et al. (2014): (1) "BD2290" for Fe,Mg-rich clays with narrow absorption near 2.29 μm (16,650 and 7305 pixels in purple, respectively), (2) "BD2210_2" for Al-rich clays with single absorption at 2.21 μm (1440 pixels in green, FRT8438 only), and (3) "BD2165" for other Al-rich clays with doublet absorptions at 2.17–2.21 μm (163 pixels in cyan, FRT8438 only). Inset (A) is a close-up view on the three phases from HiRISE image (ESP_012214_1970). CRISM spectra are compared with laboratory spectra of terrestrial analogues (nontronite, montmorillonite, illite and kaolinite). While our work is mainly focused on the Fe,Mg-rich clays, the Al-rich clays were initially identified in previous studies (Noe Dobrea et al., 2010; Turner et al., 2021) and analyzed here to complement our discussion. (For interpretation of the references to color in this figure legend, the reader is referred to the web version of this article.)

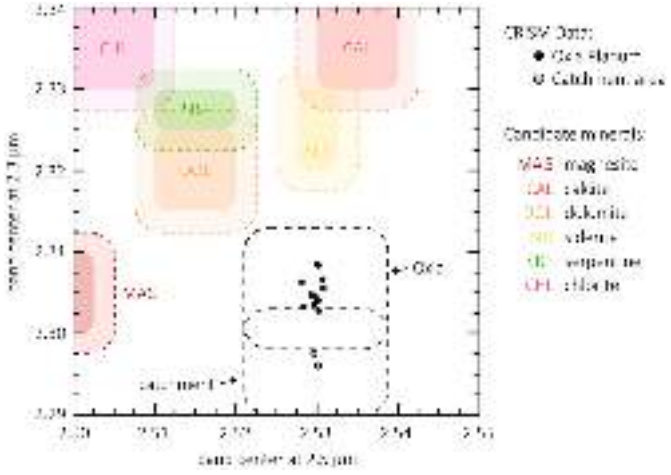

Fig. 12. Scatterplot of 2.3 μm vs 2.5 μm band centers for studied clay-bearing outcrops and candidate minerals: carbonates (siderite, magnesite, calcite and dolomite) from Gaffey (1986, 1987) and Leask et al. (2021), serpentines (lizardite and antigorite) and chlorites (clinochlore and chamosite) from King and Clark (1989); Bishop et al. (2008a, 2008b) and Ehlmann et al. (2010). Dashed outlines indicate the error areas: 2.5 nm for the candidate minerals (sampling) and standard deviations for the CRISM data (Table 2).

with a broad peak in the 3–4 μm range) supported by previous surveys done in the region (e.g., Bultel et al., 2019).

Besides the carbonates, we cannot rule out the possible presence of another phyllosilicate, such as serpentine or chlorite (e.g., Bishop et al., 2008b; Ehlmann et al., 2010; Quantin et al., 2012; Sun and Milliken, 2015). Diagnostic absorptions of serpentines are centered at 2.325 μm and 2.51–2.52 μm, in addition to the requisite 1.4 and 1.9 μm features (King and Clark, 1989). Mg-rich serpentines (e.g., antigorite, lizardite and chrysotile) are more likely to be present on Mars (e.g., Ehlmann et al., 2010; Quantin et al., 2012). They have an additional, weaker absorption near 2.10–2.12 μm, often at noise level (Fig. 13). Some cubes display a subtle absorption near 2.10–2.15 μm, notably FRT810D and FRT9A16 (see Figs. 3 and 8). No parameter maps (e.g., Viviano-Beck et al., 2014; Bultel et al., 2015b) seem to display a clear absorption near 2.1 μm that could correlate to our clay-bearing outcrops (ROIs). However, it is difficult to fully assess this feature in our data because of the strong water absorption at 1.9 μm, and the residual atmospheric CO_2 absorption at 2 μm (Murchie et al., 2007; Leask et al., 2018). Alternatively, chlorites (e.g., clinochlore and chamosite) are commonly identified with multiple absorptions centered at 1.4, 1.9, 2.25–2.26, 2.33–2.36 and 2.47–2.51 μm (King and Clark, 1989; Bishop et al., 2008b) (Fig. 13). Although we do not clearly observe any of the chlorite absorptions at the CRISM data resolution, we cannot rule out their presence in Oxia Planum.

All these candidate minerals (carbonates, serpentines and chlorites) have multiple absorptions within the 2.2–2.6 μm spectral range, making their definitive diagnostic challenging in mixture with clays. Also, the presence of one or more of these minerals could produce shifts in the band centers observed near 2.3 and 2.5 μm. Future lab experiments of mineral mixtures (e.g., spectral and XRD analyses from Bishop et al., 2013b) may provide better insights on these variations in order to facilitate mineral identification.

4.3. Ferrous component(s)

Besides the little variations seen in the four absorptions of interest (Section 4.1), the overall spectrum of the clay-bearing outcrops in Oxia Planum is almost homogeneous between 1 and 4 μm (Fig. 8). Most spectra display a positive and concave upward slope in the 1–2 μm region, followed by a reflectance drop near 2.3 μm. Such a slope results from multiple broad absorptions due to electronic excitations of Fe^{2+} occurring between 0.95 and 1.3 μm, and hereafter refers as a "ferrous slope" (e.g., Burns, 1993; Morris et al., 1982; Sunshine and Pieters, 1998). Similar observations have been reported in previous surveys on the Mawrth Vallis – west Arabia Terra province (e.g., Bishop et al., 2008a; McKeown et al., 2009; Noe Dobrea et al., 2010). Authors argue that this slope can be attributed to a ferrous (Fe^{2+}) bearing component present in the mineral assemblage, such as olivine, ferrous carbonate (e.g., siderite) or even ferrous micas (e.g., biotite, glauconite, celadonite) and ferrous chlorites (e.g., chamosite).

Moreover, a small outcrop seen in the ATU38B10 cube (near *Raetia Palus*) shows a very strong slope with a convex shape near 1.4 μm (light blue spectrum in Fig. 8). Unlike the other outcrops, it has a bluish appearance (Fig. 7C), and may correspond to the "blue unit" defined in Mandon et al. (2021). They propose that a Fe-rich olivine (fayalite) or a coarse-grained Mg-rich olivine (forsterite) in mixture with clays is more likely to produce the convex downward shape in the spectrum. They also show that the clay absorptions are weaker with respect to other clay-bearing outcrops, while the olivine slope remains on the surrounding areas farther out from the small outcrop in this cube (their Fig. 9). Fig. 15 shows that the olivine-rich areas correlate well with the clay-bearing outcrops, as suggested in Mandon et al. (2021) and Condus (2022). Bishop et al. (2013b) found that small amounts of olivine (only 10 wt%) in mixtures with clays and carbonates are enough to contribute greatly toward the ferrous slope. As for the other outcrops, where no apparent olivine-rich areas are detected, Fe-rich carbonates (siderite) can also contribute to the positive slope observed in our spectra (see Section 4.2).

Alternatively, ferrous micas, such as biotite, also display a broad Fe^{2+} absorption in the 1 μm spectral region resulting in a positive, concave up slope in the 1–2 μm region (Clark et al., 1990). Biotite (or phlogopite) is often found in association with vermiculite, as the latter is a common weathering product of biotite in terrestrial basalts (e.g., Velde, 1978; Swayze et al., 2009; 2018). Furthermore, the presence of biotite with vermiculite can explain the subtle variations in band centers observed near 2.3 μm (Fig. 9), as biotite has an absorption at 2.32 μm whereas pure vermiculite shows an absorption at 2.30 μm (e.g., Clark et al., 1990).

4.4. Diverse clays: origin(s) and implications

As discussed in Section 4.1, Oxia's clays have signatures characteristic of Fe-rich saponites and vermiculites, and their spectra are essentially uniform at CRISM resolution (Figs. 8 and 9). Clay minerals may be either (1) authigenic where they have formed in situ within Oxia Planum system, or (2) detrital where they have formed elsewhere within the Mawrth Vallis – west Arabia Terra province and subsequently transported through the Coogoon Valles system. The lack of vermiculite-saponite clays detected elsewhere on the surrounding plateaus, where the nontronite clays are predominant, is favoring the in situ formation for Oxia's clays. Nonetheless, some vermiculite-saponite clays (i.e.,

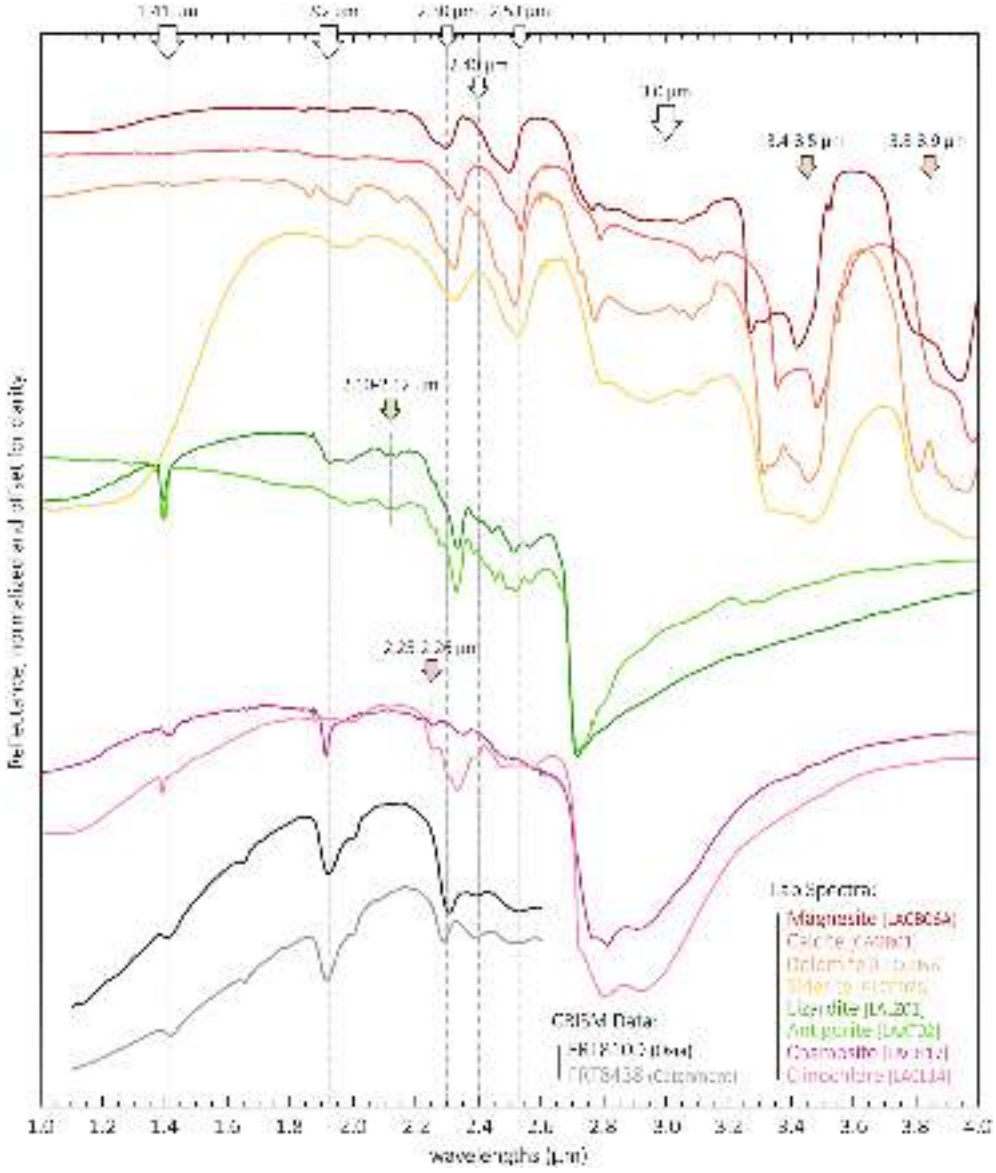

Fig. 13. Laboratory spectra of main candidate carbonates (magnesite, calcite, dolomite and siderite), serpentines (lizardite and antigorite), and chlorites (chamosite and clinochlore). All major absorptions are shown with vertical lines at 1.41, 1.92, 2.30, 2.40 and 2.53 µm. Colored arrows indicate specific absorptions associated with carbonates (3.4–3.5 µm and 3.8–3.9 µm), serpentines (2.10–2.12 µm) and chlorites (2.25–2.26 µm).

ATU4096B cube) are located on a high elevated area, forming a 'belvedere' in eastern Oxia Planum (right part of Fig. 6), which appears to be dissected by the northern channel of the Coogoon Valles system. This suggests that these outcrops predate the incision of the channel, and perhaps part of them may have been transported and deposited within Oxia's basin (Ivanov et al., 2020; Fawdon et al., 2021a).

Extensive outcrops found in the catchment area indicate different clay mineralogies, corresponding to nontronites together with Al-rich phases (montmorillonite and kaolinite) (Fig. 11). This correlates well with the previous clay detections reported in the vicinity of Mawrth Vallis and west Arabia Terra (e.g., Loizeau et al., 2007; Bishop et al., 2008a, 2008b; McKeown et al., 2009; Noe Dobrea et al., 2010). At first glance, these materials could have been deposited within Oxia's basin after transportation through the Coogoon Valles system (Turner et al., 2021). However, regarding our results, these isolated outcrops do not appear to be associated with the vermiculite-saponite clays identified in Oxia Planum. Distinct clay mineralogies in the two regions could denote differences in the weathering processes and conditions occurring during the formation of the clay minerals.

Distribution of the clay minerals in the catchment area, with Al-rich clays lying above Fe,Mg-rich clays, strongly resembles to vertical sequences initially described in Mawrth Vallis (e.g., Loizeau et al., 2010) and near Valles Marineris (e.g., Le Deit et al., 2012). Indeed, long-term weathering may produce vertical sequences where Al-rich phases overlie thicker piles of Fe,Mg-rich clays (e.g., Loizeau et al., 2015, 2018; Bultel et al., 2019) (see also Fig. 16). On Earth, such clay sequences indicate surface weathering under humid climates, and can be related to pedogenic sequences (e.g., Velde, 2010; Gaudin et al., 2011). Pedogenesis (or soil formation) consists on the leaching of soil horizons (here Noachian basaltic crust) due to water percolating from top to bottom (e.g., Gaudin et al., 2011), analogous to basaltic andosols on Earth (e.g., Quantin, 1972; Chamley, 1989). Al cations are less mobile than Fe and Mg cations and therefore remain generally in the upper part of the pedogenic sequence, where the drainage is intense and Al-rich clays and kaolins form (e.g., Loizeau et al., 2007; Le Deit et al., 2012; Carter et al., 2015b). Conversely, Fe and Mg cations migrate downward and accumulate in the poorly drained, lowest part of the weathering profile, where the Fe,Mg-rich clays form in a neutral to alkaline environment (e.

Table 4
Absorption band centers for clay-bearing outcrops in Oxia Planum and within its catchment area, as well as candidate materials in the 1.4, 2.3, 2.4 and 2.5 μm windows. Notes: [1] Clark et al. (1990); Bishop et al. (2013a) for saponite and nontronite, Treiman et al. (2014) for Fe-bearing saponite (i.e., Griffithite), and Swayze et al. (2018a) for vermiculite ore (vermiculite and hydrobiotite). [2] Gaffey (1986, 1987) and Leask et al. (2021) for carbonates. [3] King and Clark (1989); Bishop et al. (2008a, 2008b) and Ehlmann et al. (2010) for serpentines and chlorites.

Materials	1.4 μm	2.3 μm	2.4 μm	2.5 μm
Oxia (our study)	1.409 ± 0.007	2.306 ± 0.008	2.397 ± 0.009	2.530 ± 0.009
Catchment (our study)	1.412 ± 0.008	2.296 ± 0.006	2.397 ± 0.008	2.530 ± 0.009
Clays[1]				
Saponite	1.380–1.390	2.310–2.320	2.380–2.390	
Nontronite	1.410–1.420	2.280–2.290	2.400–2.410	
Fe-saponite	1.405–1.415	2.300–2.315	2.395–2.400	
Vermiculite ore	1.400–1.420	2.300–2.320	2.380–2.390	
Vermiculite (flake)	1.420	2.300–2.310	2.390	
Hydrobiotite (flake)	1.400	2.320	2.380	
Carbonates[2]				
Siderite		2.320–2.330		2.530
Magnesite		2.300–2.310		2.500
Dolomite		2.315–2.325		2.510–2.520
Calcite		2.330–2.340		2.530–2.540
Serpentines[3]				
Lizardite	1.395	2.325		2.510
Antigorite	1.395	2.325		2.520
Chlorites[3]				
Clinochlore	1.390	2.330		2.470
Chamosite	1.415	2.360		2.510

g., Gaudin et al., 2011). Note that nontronites are Al,Fe-rich clays, and hence, should be forming in an intermediate horizon (or layer) between the Al-rich phases (on top) and the Fe,Mg-rich phases (at the bottom) (Fig. 16).

Oxia's clay-bearing outcrops are relatively homogeneous over tens of meters of thickness (Mandon et al., 2021; this study), and the absence of such a vertical sequence in the basin tends to favor alternative origins such as formation within subaqueous environments (notably lacustrine and deltaic systems), hydrothermal or groundwater systems, rather than pedogenesis (Quantin-Nataf et al., 2021; Mandon et al., 2021). Like in aforementioned studies, our current observations and results do not allow us to confidently discriminate among the different scenarios for the formation and evolution of the clays in the region. Nevertheless, clay-bearing outcrops present within Oxia's basin may belong to the lower horizon of the pedogenic sequence (i.e., Fe,Mg-rich phases) described near Mawrth Vallis (e.g., Loizeau et al., 2015, 2018), while the outcrops identified in the catchment represent the upper horizons (i.e., Al-rich phases above Al,Fe-rich phases) (Fig. 16). As mentioned in Mandon et al. (2021), the lack of authigenic Al-rich phases (e.g., montmorillonite, kaolinite) and Al,Fe-rich phases (nontronite) in Oxia Planum, could be due to a moderate leaching intensity during the pedogenesis alteration, or that any horizons corresponding to these phases have been removed by the significant erosion occurring in the region (Favaro et al., 2021; Quantin-Nataf et al., 2021; Silvestro et al., 2021). Reader is referred to Quantin-Nataf et al. (2021) and Mandon et al. (2021) for further discussion regarding the different geological environments that possibly occurred in Oxia Planum and its surroundings.

Fe,Mg-rich phyllosilicates (particularly nontronites, saponites and vermiculites) are generally surface and shallow subsurface clay minerals, resulting from the interaction of liquid water with rocks under low temperatures, moderate pH levels and reducing conditions, factors in favor for life (Velde, 2010; Gaudin et al., 2011). On Earth, clay minerals (e.g., in marine and deltaic sediments) played an active role for the emergence of life, as they can store organic carbon over geologic timescales (e.g., Hays et al., 2017). ExoMars "Rosalind Franklin" rover and its plethora of instruments are designed to collect and analyze surface and subsurface samples (rocks and soils) down to 2 m in depth (Vago et al., 2017), where organic compounds may be better conserved. Indeed, subsurface samples are more likely to include biosignatures, since the tenuous atmosphere of Mars offers little protection from radiation and photochemistry at the surface.

Presence of additional spectral features suggests the co-occurrence of carbonates throughout the clay-bearing outcrops (Section 4.2), with a broad absorption near 2.5 μm and a strong 3.9 μm-index (Fig. 8). Interestingly, carbonates are also reported in the weathering profiles previously discussed, where they are collocated with the clays near Mawrth Vallis and west Arabia Terra province (Bultel et al., 2019). The stratigraphy observed in these profiles (from Al-rich phases on top to Fe, Mg-rich phases at the bottom) together with the precipitation of carbonates (in the middle sections), indicates a pH gradually increasing from the top (acidic) to the bottom (neutral to alkaline) of the vertical sequence (Gaudin et al., 2011; Zolotov and Mironenko, 2016). Fig. 16 is a sketch illustrating the stratigraphic column induced by a possible pedogenesis alteration scenario occurring in Oxia Planum and its surroundings (after Bultel et al., 2019). Precipitation of carbonates generally implies that neutral-to-alkaline waters circulated at the time of their formation, coinciding with the formation of Fe,Mg-rich clays during the Noachian era. Furthermore, their presence indicates that they have been protected from any acidic (sulfate-forming) environments characteristic of the Hesperian era (e.g., Bibring et al., 2006; Hurowitz and McLennan, 2007), which would have dissolved them. Thus, the coprecipitation of clay minerals and carbonates throughout the studied outcrops in Oxia's basin and its catchment further strengthens the exobiological potential of the region, where biosignatures might still be preserved.

5. Conclusions

We provide an in-depth analysis of the clay-bearing outcrops found in Oxia Planum, to complement previous surveys (Carter et al., 2016; Mandon et al., 2021) and better constrain the nature of the minerals present in the region. We propose a more detailed spectral analysis of the CRISM infrared data aiming to: (1) report exact positions of the 1.4, 2.3, 2.4 and 2.5 μm band centers, (2) locate possible shifts in band centers within the outcrops' spectra, and (3) better characterize the 3–4 μm spectral region to search carbonate features. We also identify and map the distribution of the "purest" exposures of clays in the area, as defined by the deepest absorptions at 1.9 and 2.3 μm. The outcrops (and major geologic units) are made accessible to the community as shapefiles via the online repository linked to this work (Brossier et al., 2022). Our analysis indicates that most of Oxia's clays are consistent with Fe-rich saponites (e.g., Griffithite or Griffith saponite) or perhaps vermiculite ores (associated with a hydrobiotite component). Spectral signatures show very subtle variations between the different targeted regions (ROIs) at the scale of orbital data, indicating a relatively homogeneous distribution of the mineral assemblage, with very little changes in Fe^{2+} (ferrous), Fe^{3+} (ferric) and Mg content. Striking differences in the spectral features are observed in the large and isolated clay-bearing outcrops identified in the catchment area, suggesting the presence of nontronites and some Al-rich phases (e.g., montmorillonites, kaolinites) in this region.

A possible mixture with carbonates, serpentines and/or chlorites is also addressed. However, it is challenging to ascertain their presence since they all have spectral features occurring in the 2.2–2.6 μm range, like the clays. Additionally, the presence of instrument artifacts and residual atmospheric absorptions make this assessment even more

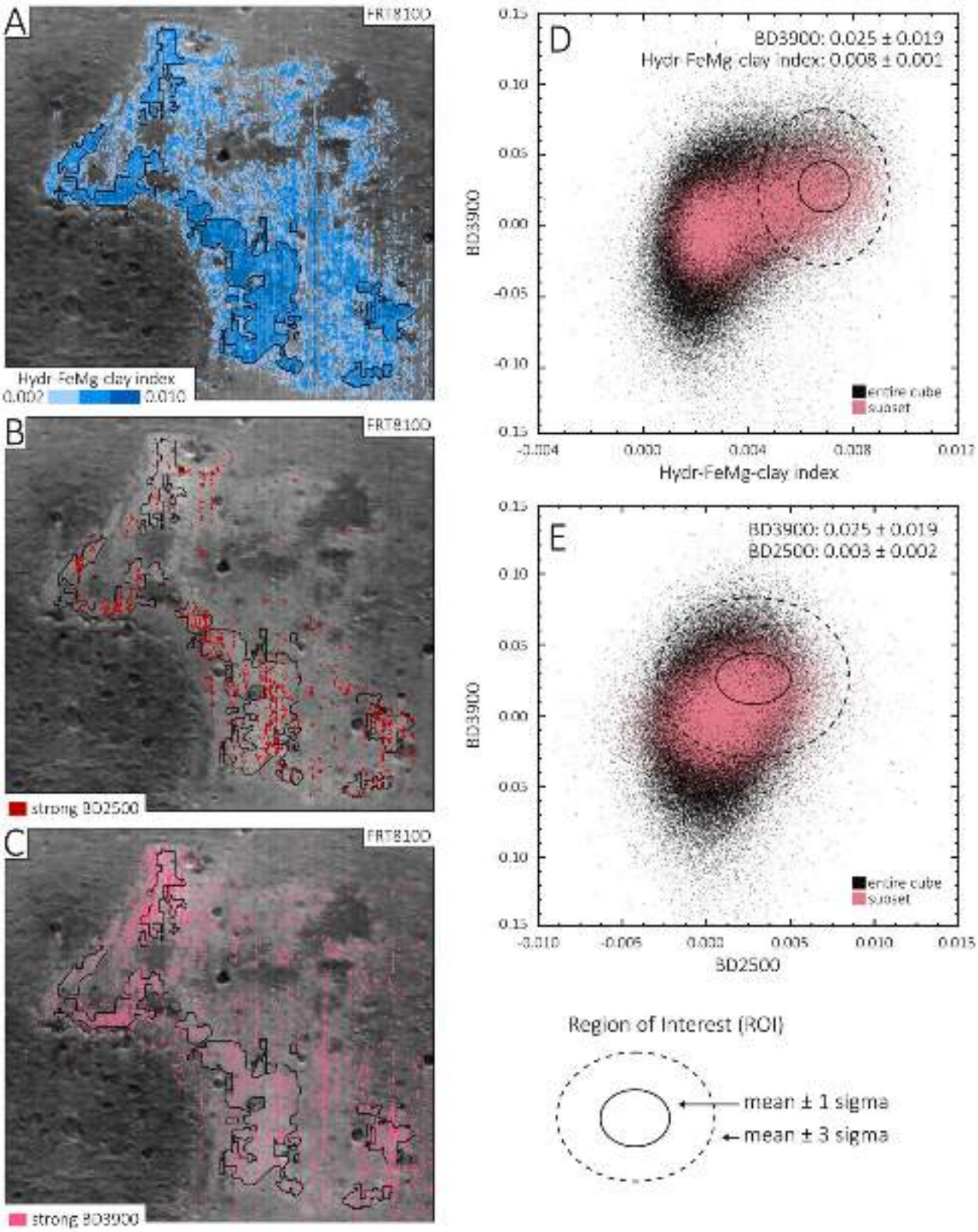

Fig. 14. (left) Subsets of band parameters covering the outcrop in FRT810D cube. (A) "Hydr-FeMg-clay index" to outline the Fe,Mg-rich clay-bearing outcrops (Loizeau et al., 2018), (B) "BD2500" to show the shallow band depth near 2.5 μm (Viviano-Beck et al., 2014), and (C) "BD3900" to show the drop of reflectance near 3.9 μm (Ehlmann et al., 2008a). (right) Scatterplots comparing the three parameters: (D) BD3900 vs Fe,Mg-rich clay index, and (E) BD3900 vs BD2500. They indicate a possible correlation between the clay features (combined absorptions at 1.41, 1.92, 2.30 and 2.40 μm) and the carbonate features (absorption at 2.53 μm and broad peak near 3.6–3.7 μm).

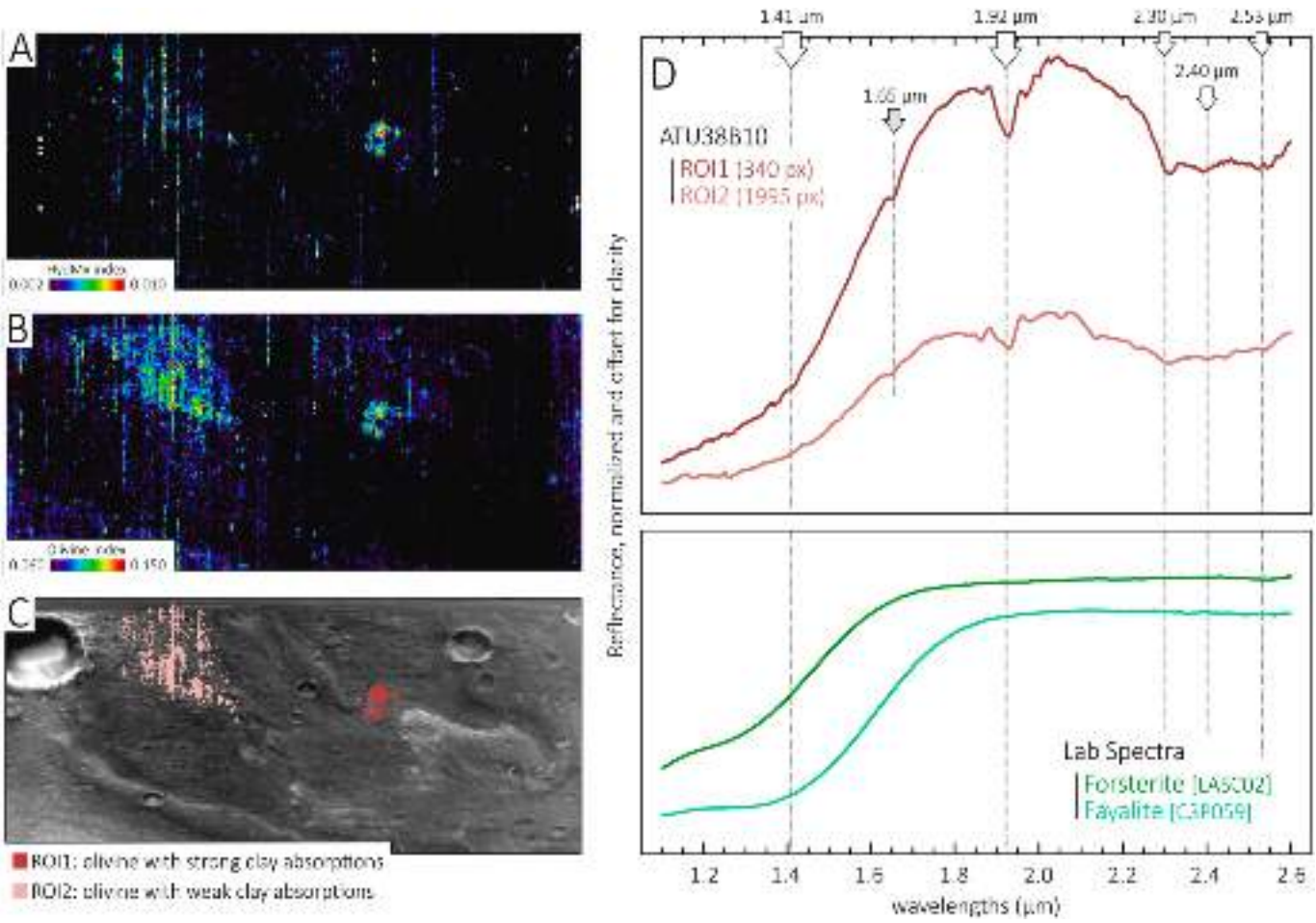

Fig. 15. Band parameters covering the outcrop in ATU38B10 cube: (A) "Hydr-FeMg-clay index" to outline the clay-bearing outcrops (Loizeau et al., 2018) and (B) "OLINDEX3" to show the olivine-rich areas (Viviano-Beck et al., 2014). (C) Two major outcrops mapped as regions of interest (ROIs). Both show strong olivine absorption near 1 µm, while one is having strong clay absorptions (ROI_1) and another has weak clay absorptions (ROI_2). (D) Denoised reflectance spectra of the two outcrops compared with two laboratory spectra of olivine (fayalite and forsterite). Although the clay signal is weaker in ROI_2, the absorptions near 1.9 and 2.3 µm are still present.

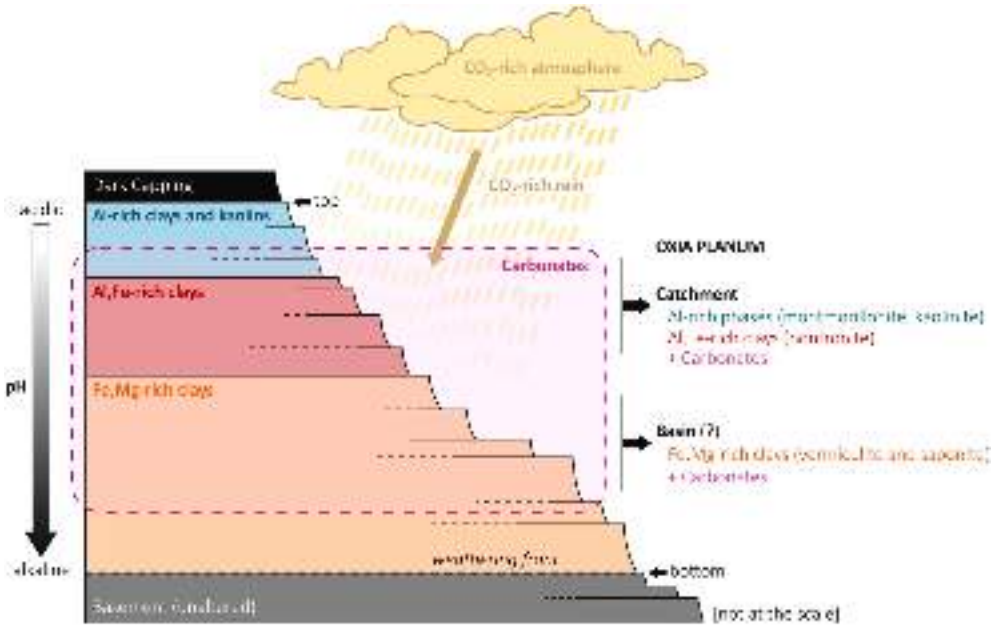

Fig. 16. Sketch of the stratigraphic column (vertical sequence) for a possible pedogenesis alteration scenario in Oxia Planum and its surroundings (adapted from Bultel et al., 2019): Al-rich clays and kaolins on top (e.g., montmorillonite, kaolinite), Al,Fe-rich clays in an intermediate horizon (e.g., nontronite), and Fe,Mg-rich clays at the bottom (e.g., saponites and vermiculites). The pedogenic weathering of the soil also involves an increase in the pH from slightly acidic near the surface to neutral - alkaline near the weathering front, where the Fe,Mg-rich clays form. Carbonates are found in different horizons like in the weathering profiles described in Mawrth Vallis, and suggest a denser CO_2-rich atmosphere at the time of their formation during or after the formation of the clay minerals.

difficult. Nevertheless, the 3.9 μm index has been computed and mapped to specifically investigate the carbonates. Our results show that the studied outcrops have a quite high index, and together with the ubiquitous absorption near 2.53 μm, strongly support the co-occurrence of carbonates with the clays in Oxia's basin and its catchment area.

Different scenarios have been discussed to explain the formation and alteration of Oxia's clays, at local scale (Mandon et al., 2021; Quantin-Nataf et al., 2021) and regional scale (e.g., McKeown et al., 2009; Noe Dobrea et al., 2010). Previous studies suggest: (1) subaqueous sedimentation (fluvial and lacustrine scenarios), (2) pedogenesis (soil formation), and (3) groundwater alteration. Whilst we favor a pedogenesis origin for the clay minerals identified in the catchment area, assessing the origin of those studied in Oxia's basin is a difficult task. Most suitable alteration scenarios in Oxia's basin could be also pedogenesis alteration, given the regional context with west Arabia Terra. However, orbital data do not provide enough constraints to discriminate among the possible scenarios (lacustrine and deltaic sedimentation, or even groundwater circulation), and therefore the origin(s) of Oxia's clays remain(s) uncertain. On Earth, Fe-rich clays are found in a broad range of geologic environments: from lacustrine and marine sediments (e.g., Müller and Förstner, 1976; Pedro et al., 1978) to seafloor hydrothermal deposits associated with microbial forms (e.g., Dekov et al., 2007; Ta et al., 2017). In Oxia Planum, observations reported in previous studies (Mandon et al., 2021; Quantin-Nataf et al., 2021) are confined in a localized area, namely Pannonia Planitia (Fig. 7, top left), and they need to be verified elsewhere in the region. Nonetheless, further detailed investigations are therefore required concerning the geologic features associated with the clays in Oxia Planum and surroundings (e.g., fractures in Apuzzo et al., 2021, 2022; Parkes-Bowen et al., 2022).

Spectra analyzed here are the best available orbital data to constrain the mineralogy of Oxia Planum and before the landing of ExoMars "Rosalind Franklin" rover, no better data are expected from the ongoing missions. For this reason, further analysis of all available data in a synergic way is desirable. Moreover, laboratory studies on terrestrial minerals and mixtures comparable to those expected at Oxia are required for further constraining the origin and evolution of the landing area. It is worth noting that the mission will conduct a detailed investigation of the area at a spatial scale extremely different (from meters to microns) relative to orbital data (up to tens of meters). Thus we would expect a much larger variety of minerals and must be prepared for the interpretation of the data at such a detailed scale. In labs, terrestrial analogues are being analyzed to test and prepare the nine instruments for "Rosalind Franklin" rover (Vago et al., 2017), including Ma_MISS (De Sanctis et al., 2017, 2022) or even MicrOmega (Bibring et al., 2017). Ma_MISS will investigate the subsurface mineralogy in its stratigraphic context and, with the other rover instruments, can gather data to understand the origin(s) of the minerals in Oxia and their weathering history. MicrOmega will characterize the texture and composition of minerals and organic compounds with astrobiological relevance.

Data availability statement

CRISM, THEMIS and HiRISE datasets are available through the NASA PDS server (https://ode.rsl.wustl.edu/mars/), while CTX and CaSSIS mosaics covering Oxia Planum are accessible from Fawdon et al. (2021b) and described therein. Besides images, all shapefiles (with auxiliary files) and tables of values used for the figures are stored in the online repository linked to this work (Brossier et al., 2022).

Declaration of Competing Interest

None.

Acknowledgments

This work is fully funded and supported by the Italian Space Agency (ASI) [Grant ASI-INAF n. 2017–48–H.0]. We are greatly thankful to the CRISM team for the CAT tool, and European Space Agency (ESA) and Russian Space Agency ROSCOSMOS for the ExoMars project. We thank the two reviewers for their thoughtful and thorough comments that significantly improved the manuscript.

Appendix A. Supplementary data

Supplementary data to this article can be found online at https://doi.org/10.1016/j.icarus.2022.115114.

References

Apuzzo, A., et al., 2021. Tectonic-related fractures in Oxia Planum (Mars) and their implications for life investigation. In: 52nd LPSC Abstracts, p. 2082.
Apuzzo, A., et al., 2022. Fractured regions of ExoMars 2022 landing site: Mapping of the fractured regions. In: 53rd LPSC Abstracts, p. 2115.
Bibring, J.-P., et al., 2004. OMEGA: Observatoire pour la Minéralogie, l'Eau, les Glaces et l'Activité. In: Wilson, A., Chicarro, A. (Eds.), Mars Express: The Scientific Payload, pp. 37–49 volume 1240 of ESA Special Publication, August, Noordwijk, The Netherlands.
Bibring, J.-P., et al., 2005. Mars surface diversity as revealed by the OMEGA/Mars express observations. Science 307, 1576–1581. https://doi.org/10.1126/science.1108806.
Bibring, J.-P., et al., 2006. Global mineralogical and aqueous mars history derived from OMEGA/Mars express data. Science 312, 400–404. https://doi.org/10.1126/science.1122659.
Bibring, J.-P., et al., 2017. The MicrOmega investigation onboard ExoMars. Astrobiology 17 (6–7), 621–626. https://doi.org/10.1089/ast.2016.1642.
Bishop, J.L., et al., 2008a. Phyllosilicate diversity and past aqueous activity revealed at Mawrth Vallis. Mar. Sci. 321, 830. https://doi.org/10.1126/science.1159699.
Bishop, J.L., et al., 2008b. Reflectance and emission spectroscopy study of four groups of phyllosilicates: smectites, kaolinite-serpentines, chlorites and micas. Clay Miner. 43, 35–54. https://doi.org/10.1180/claymin.2008.043.1.03.
Bishop, J.L., et al., 2010. Mineralogy of Lybia Montes and the southern Isidis Planitia region: CRISM detection of clay, carbonate, olivine and pyroxene, and correlation with HiRISE imagery. In: 41st LPSC Abstracts, p. 2147.
Bishop, J.L., et al., 2013a. Mineralogy and morphology of geologic units at Lybia Montes, Mars: ancient aqueously derived outcrops, mafic flows, fluvial features, and impacts. JGR Planets 118, 487–513. https://doi.org/10.1029/2012JE004151.
Bishop, J.L., Perry, K.A., Dyar, M.D., et al., 2013b. Coordinated spectral and XRD analyses of magnesite-nontronite-forsterite mixtures and implications for carbonates on Mars. JGR Planets 118, 635–650. https://doi.org/10.1002/jgre.20066.
Blaney, D.L., McCord, T.B., 1989. An observational search for carbonates on Mars. JGR Solid Earth 94, 10,159–10,166. https://doi.org/10.1029/JB094iB08p10159.
Brindley, G.W., Zalba, Patricia E., Craig, M., 1983. Bethke (1983); Hydrobiotite, a regular 1: 1 interstratification of biotite and vermiculite layers. American Mineralogist 68 (3-4), 420–425.
Brossier, J., et al., 2021. Reconstructing the infilling history within Robert Sharp crater, Mars: insights from morphology and stratigraphy. Icarus 358, 114223. https://doi.org/10.1016/j.icarus.2020.114223.
Brossier, J., et al., 2022. Constraining the Spectral Behavior of the Clay-Bearing Outcrops in Oxia Planum, the Landing Site for ExoMars 2022 "Rosalind Franklin" Rover: Supporting Datasets. https://doi.org/10.6084/m9.figshare.18893906.v2.
Bultel, B., Quantin, C., Lozach, L., 2015a. Description of CoTCAT (complement to CRISM analysis toolkit). IEEE J. Sel. Top. Appl. Earth Obs. Remote Sens. 8, 3039–3049. https://doi.org/10.1109/JSTARS.2015.2405095.
Bultel, B., Quantin-Nataf, C., Andréani, M., Clénet, H., Lozac'h, L., 2015b. Deep alteration between Hellas and Isidis basins. Icarus 260, 141–160. https://doi.org/10.1016/j.icarus.2015.06.037.
Bultel, B., et al., 2019. Detection of carbonates in Martian weathering profiles. JGR Planets 124, 989–1007. https://doi.org/10.1029/2018JE005845.
Burns, R.G., 1993. Mineralogical Applications of Crystal Field Theory, 2nd ed. Cambridge Univ. Press, Cambridge, U. K. 551 pp.
Carter, J., et al., 2013. Hydrous minerals on Mars as seen by the CRISM and OMEGA imaging spectrometers: updated global view. JGR Planets 118, 831–858. https://doi.org/10.1029/2012JE004145.
Carter, J., et al., 2015a. Orbital detection and implications of akaganeite on Mars. Icarus 253, 296–310. https://doi.org/10.1016/j.icarus.2015.01.020.
Carter, J., Loizeau, D., Mangold, N., Poulet, F., Bibring, J.-P., 2015b. Widespread surface weathering on early Mars: a case for a warmer and wetter climate. Icarus 248, 373–382. https://doi.org/10.1016/j.icarus.2014.11.011.
Carter, J., et al., 2016. Oxia Planum, a clay-laden landing site proposed for the ExoMars rover mission: Aqueous mineralogy and alteration scenarios. In: 47th LPSC Abstracts, p. 2064.
Chamley, H., 1989. Clay Sedimentology, 623 Pp. Springer, New York. https://doi.org/10.1007/978-3-642-85916-8.
Chemtob, S.M., et al., 2015. Synthesis and structural characterization of ferrous trioctahedral smectites: implications for clay mineral genesis and detectability on Mars. JGR Planets 120, 1119–1140. https://doi.org/10.1002/2014JE004763.

Clark, R.N., et al., 1990. High spectral resolution reflectance spectroscopy of minerals. JGR Solid Earth 95 (B8), 12,653–12,680. https://doi.org/10.1029/JB095iB08p12653.
Clark, R.N., et al., 2007. USGS digital spectral library splib06a. In: U.S. Geological Survey, Digital Data Series, 231. http://speclab.cr.usgs.gov/spectral.lib06.
Cloutis, E.A., 2015. Mineral and rock sample database: Planetary Spectrophotometer Facility (PSF). University of Winnipeg. https://www.uwinnipeg.ca/c-tape/docs/sample-bible.pdf.
Cloutis, E.A., et al., 2007. Stability of hydrated minerals on Mars. GRL 34, L20202. https://doi.org/10.1029/2007GL031267.
Condus, T., 2022. CRISM-based mineral abundance maps for the Oxia Planum delta. In: 53rd LPSC Abstracts, p. 2528.
De Sanctis, M.C., et al., 2017. Ma_MISS on ExoMars: mineralogical characterization of the Martian subsurface. Astrobiology 17, 612–620. https://doi.org/10.1089/ast.2016.1541.
De Sanctis, M.C., et al., 2022. Exploring the shallow subsurface of Mars with the Ma_MISS spectrometer on the ExoMars Rover Rosalind Franklin. Planet. Sci. J. 3, 142. https://doi.org/10.3847/PSJ/ac694f.
Dekov, V.M., et al., 2007. Hydrothermal nontronite formation at Eolo Seamount (Aeolian volcanic arc, Tyrrhenian Sea). Chem. Geol. 245, 103–119. https://doi.org/10.1016/j.chemgeo.2007.08.006.
Delamere, W.A., et al., 2010. Color imaging of Mars by the high resolution imaging science experiment (HiRISE). Icarus 205, 38–52. https://doi.org/10.1016/j.icarus.2009.03.012.
Ehlmann, B.L., et al., 2008a. Orbital identification of carbonate-bearing rocks on Mars. Science 322, 1828–1832. https://doi.org/10.1126/science.1164759.
Ehlmann, B.L., et al., 2008b. Clay minerals in delta deposits and organic preservation potential on Mars. Nat. Geosci. 1, 355–358. https://doi.org/10.1038/ngeo207.
Ehlmann, B.L., et al., 2009. Identification of hydrated silicate minerals on Mars using MRO-CRISM: geologic context near Nili Fossae and implications for aqueous alteration. JGR Planets 114, E00D08. https://doi.org/10.1029/2009JE003339.
Ehlmann, B.L., Mustard, J.F., Murchie, S.L., 2010. Geologic setting of serpentine deposits on Mars. GRL 37, L06201. https://doi.org/10.1029/2010GL042596.
Favaro, E.A., et al., 2021. The aeolian environments of the landing site for ExoMars Rosalind Franklin rover in Oxia Planum, Mars. JGR Planets 126. https://doi.org/10.1029/2020JE006723 e2020JE006723.
Fawdon, P., et al., 2021a. Rivers and Lakes in Western Arabia Terra: The Fluvial Catchment of the ExoMars 2022 rover landing site. Earth Space Sci. Open Arch. https://doi.org/10.1002/essoar.10507896.1, 47 pp.
Fawdon, P., et al., 2021b. The geography of Oxia Planum. J. Maps 17, 752–768. https://doi.org/10.1080/17445647.2021.1982035.
Gaffey, S.J., 1986. Spectral reflectance of carbonate minerals in the visible and near infrared (0.35–2.55 μm): calcite, aragonite, and dolomite. Am. Mineral. 71 (1–2), 151–162.
Gaffey, S.J., 1987. Spectral reflectance of carbonate minerals in the visible and near infrared (0.35–2.55 μm): anhydrous carbonate minerals. JGR Solid Earth 92 (B2), 1429–1440. https://doi.org/10.1029/JB092iB02p01429.
Gaudin, A., Dehouck, E., Mangold, N., 2011. Evidence for weathering on Early Mars from a comparison with terrestrial weathering profiles. Icarus 216, 257–268. https://doi.org/10.1016/j.icarus.2011.09.004.
Hays, L.E., et al., 2017. Biosignature preservation and detection in Mars analog environments. Astrobiology 17 (4), 363–400. https://doi.org/10.1089/ast.2016.1627.
Hexter, R.M., 1958. High-resolution, temperature-dependent spectra of calcite. Spectrochim. Acta 10 (3), 281–290. https://doi.org/10.1016/0371-1951(58)80094-6.
Horgan, B.H.N., et al., 2020. The mineral diversity of Jezero crater: evidence for possible lacustrine carbonates on Mars. Icarus 339, 113526. https://doi.org/10.1016/j.icarus.2019.113526.
Hunt, G.R., 1977. Spectral signatures of particulate minerals in the visible and near infrared. Geophysics 42 (3), 501–513. https://doi.org/10.1190/1.1440721.
Hunt, G.R., Salisbury, J.W., 1971. Visible and near infrared spectra of minerals and rocks. II. Carbonates. Mod. Geol. 2, 23–30.
Hurowitz, J.A., McLennan, S.M., 2007. A ~3.5 Ga record of water-limited, acidic weathering conditions on Mars. EPSL 260, 432–443. https://doi.org/10.1016/j.epsl.2007.05.043.
Ivanov, M.A., et al., 2020. Geomorphological analysis of ExoMars candidate landing site Oxia Planum. Sol. Syst. Res. 54, 1–14. https://doi.org/10.1134/S0038094620010050.
King, T.V., Clark, R.N., 1989. Spectral characteristics of chlorite and Mg-serpentines using high-resolution reflectance spectroscopy. JGR Solid Earth 94, 13,997–14,008. https://doi.org/10.1029/JB094iB10p13997.
Kirk, R.L., et al., 2009. Ultrahigh resolution topographic mapping of Mars with MRO HiRISE stereo images: meter-scale slopes of candidate Phoenix landing sites. JGR Planets 113, E00A24. https://doi.org/10.1029/2007JE003000.
Kokaly, R.F., et al., 2017. USGS Spectral Library Version 7. U.S. Geological Survey Data Series 1035, 61 pages. https://doi.org/10.3133/ds1035.
Krzesińska, A.M., et al., 2021. Mineralogical and spectral (near-infrared) characterization of Fe-rich vermiculite-bearing terrestrial deposits and constraints for mineralogy of Oxia Planum, ExoMars 2022 landing site. Astrobiology 21, 997–1016. https://doi.org/10.1089/ast.2020.2410.
Le Deit, L., et al., 2012. Extensive surface pedogenic alteration of the Martian Noachian crust suggested by plateau phyllosilicates around Valles Marineris. JGR Planets 117, E00J05. https://doi.org/10.1029/2011JE003983.
Leask, E.K., et al., 2018. Challenges in the search for perchlorate and other minerals with 2.1-μm absorptions on Mars. GRL 45, 12,180–12,189. https://doi.org/10.1029/2018GL080077.
Leask, E.K., et al., 2021. Tracing carbonate formation, serpentinization, and biological materials with micro−/meso-scale infrared imaging spectroscopy in a Mars analogue system, Samail Ophiolite, Oman. Earth Space Sci. 8 https://doi.org/10.1029/2021EA001637 e2021EA001637.
Loizeau, D., et al., 2007. Phyllosilicates in the Mawrth Vallis region on Mars. JGR Planets 112, E08S08. https://doi.org/10.1029/2006JE002877.
Loizeau, D., et al., 2010. Stratigraphy in the Mawrth Vallis region through OMEGA, HRSC color imagery and DTM. Icarus 205, 396–418. https://doi.org/10.1016/j.icarus.2009.04.018.
Loizeau, D., et al., 2015. History of the clay-rich unit at Mawrth Vallis, Mars: high-resolution mapping of a candidate landing site. JGR Planets 120, 1820–1846. https://doi.org/10.1002/2015JE004894.
Loizeau, D., et al., 2018. Quantifying widespread aqueous surface weathering on Mars: the plateaus south of Coprates Chasma. Icarus 302, 451–469. https://doi.org/10.1016/j.icarus.2017.11.002.
Malin, M.C., et al., 2007. Context camera investigation on board the Mars reconnaissance orbiter. JGR Planets 112, E05S04. https://doi.org/10.1029/2006JE002808.
Mandon, L., et al., 2021. Morphological and spectral diversity of the clay-bearing unit at the ExoMars landing site Oxia Planum. Astrobiology 21, 464–480. https://doi.org/10.1089/ast.2020.2292.
McEwen, A.S., et al., 2007. Mars reconnaissance orbiter's high resolution imaging sciences experiment (HiRISE). JGR Planets 112, E05S02. https://doi.org/10.1029/2005JE002605.
McEwen, A.S., et al., 2010. The high resolution imaging science experiment (HiRISE) during MRO's primary science phase (PSP). Icarus 205, 2–37. https://doi.org/10.1016/j.icarus.2009.04.023.
McGuire, P.C., et al., 2009. An improvement to the volcano-scan algorithm for atmospheric correction of CRISM and OMEGA spectral data. PSS 57, 809–815. https://doi.org/10.1016/j.pss.2009.03.007.
McKeown, N.K., et al., 2009. Characterization of phyllosilicates observed in the central Mawrth Vallis region, Mars, their potential formational processes, and implications for past climate. JGR Planets 114, E00D10. https://doi.org/10.1029/2008JE003301.
McNeil, J.D., et al., 2021. Morphology, morphometry and distribution of isolated landforms in southern Chryse Planitia, Mars. JGR Planets 126. https://doi.org/10.1029/2020JE006775 e2020JE006775.
Michalski, J.R., Niles, P.B., 2010. Deep crustal carbonate rocks exposed by meteor impact on Mars. Nat. Geosci. 3, 751–755. https://doi.org/10.1038/ngeo971.
Michalski, J.R., et al., 2015. Constraints on the crystal-chemistry of Fe/Mg-rich smectite clays on Mars and link to global alteration trends. EPSL 427, 215–225. https://doi.org/10.1016/j.epsl.2015.06.020.
Michalski, J.R., et al., 2019. The geology and astrobiology of McLaughlin crater, Mars: an ancient lacustrine basin containing turbidites, mudstones, and serpentinites. JGR Planets 124, 910–940. https://doi.org/10.1029/2018JE005796.
Molina, A., et al., 2017. Coogoon Valles, western Arabia Terra: hydrological evolution of a complex Martian channel system. Icarus 293, 27–44. https://doi.org/10.1016/j.icarus.2017.04.002.
Morgan, M.F., et al., 2011. Improved algorithm for CRISM volcano scan atmospheric correction. In: 42th LPSC Abstracts, p. 2453.
Morgan, M.F., Seelos, F.P., Murchie, S.L., 2017. The CRISM Analysis Toolkit (CAT): Overview and recent updates. In: 3rd Planetary Data Workshop, p. 7121.
Morris, R.V., Neely, S.C., Mendell, W.W., 1982. Application of Kubelka-Munk theory of diffuse reflectance to geologic problems: the role of scattering. GRL 9 (2), 113–116. https://doi.org/10.1029/GL009i002p00113.
Müller, G., Förstner, U., 1976. Primary nontronite from the Venezuelan Guayana: additional primary occurrences (Red Sea, Lake Malawi). Am. Mineral. 61, 500–501.
Murchie, S.L., et al., 2007. Compact reconnaissance imaging spectrometer for Mars (CRISM) on Mars reconnaissance orbiter (MRO). JGR Planets 112, E05S03. https://doi.org/10.1029/2006JE002682.
Murchie, S.L., et al., 2009. Compact reconnaissance imaging spectrometer for Mars investigation and data set from the Mars reconnaissance orbiter's primary science phase. JGR Planets 114, E00D07. https://doi.org/10.1029/2009JE003344.
Mustard, J.F., 1992. Chemical analysis of actinolite from reflectance spectra. Am. Mineral. 77 (3–4), 345–358.
Noe Dobrea, E.Z., et al., 2010. Mineralogy and stratigraphy of phyllosilicate-bearing and dark mantling units in the greater Mawrth Vallis/West Arabia Terra area: constraints on geological origin. JGR Planets 115, E00D19. https://doi.org/10.1029/2009JE003351.
Pan, L., et al., 2021. Voluminous silica precipitated from Martian waters during late-stage aqueous alteration. PSJ 2 (2), 2–65. https://doi.org/10.3847/PSJ/abe541.
Parente, M., Clark, J., Brown, A.J., Bishop, J.L., 2010. End-to-end simulation and analytical model of remote-sensing systems: application to CRISM. IEEE Trans. Geosci. Remote Sens. 48 (11), 3877–3888. https://doi.org/10.1109/TGRS.2010.2050000.
Parkes-Bowen, A., et al., 2022. A CaSSIS and HiRISE map of the clay-bearing unit at the ExoMars 2022 landing site in Oxia Planum. PSS 214, 105429. https://doi.org/10.1016/j.pss.2022.105429.
Pedro, G., Carmouze, J.P., Velde, B., 1978. Peloidal nontronite formation in recent sediments of Lake Chad. Chem. Geol. 23, 139–149. https://doi.org/10.1016/0009-2541(78)90071-2.
Pelkey, S.M., et al., 2007. CRISM multispectral summary products: parameterizing mineral diversity on Mars from reflectance. JGR Planets 112, E08S14. https://doi.org/10.1029/2006JE002831.

Quantin, P., 1972. Les andosols: Revue bibliographique des connaissances actuelles. Cah. ORSTOM Sec. Pedol. 10 (3), 273–301.
Quantin, C., et al., 2012. Composition and structures of the subsurface in the vicinity of Valles Marineris as revealed by central uplifts of impact craters. Icarus 221, 436–452. https://doi.org/10.1016/j.icarus.2012.07.031.
Quantin-Nataf, C., et al., 2019. Decline of crater obliteration rates during early Martian history. Icarus 317, 427–433. https://doi.org/10.1016/j.icarus.2018.08.005.
Quantin-Nataf, C., et al., 2021. Oxia Planum : the landing site for the ExoMars "Rosalind Franklin" rover mission: geological context and prelanding interpretation. Astrobiology 21, 345–366. https://doi.org/10.1089/ast.2019.2191.
Silvestro, S., et al., 2021. Periodic bedrock ridges at the ExoMars 2022 landing site: evidence for a changing wind regime. GRL 48. https://doi.org/10.1029/2020GL091651 e2020GL091651.
Sun, V.Z., Milliken, R.E., 2015. Ancient and recent clay formation on Mars as revealed from a global survey of hydrous minerals in crater central peaks. JGR Planets 120, 2293–2332. https://doi.org/10.1002/2015JE004918.
Sunshine, J.M., Pieters, C.M., 1998. Determining the composition of olivine from reflectance spectroscopy. JGR Planets 103 (E6), 13,675–13,688. https://doi.org/10.1029/98JE01217.
Sutter, B., Dalton, J.B., Ewing, S.A., Amundson, R., McKay, C.P., 2007. Terrestrial analogs for interpretation of infrared spectra from the Martian surface and subsurface: sulfate, nitrate, carbonate, and phyllosilicate-bearing Atacama Desert soils. JGR Biogeosci. 112, G04S10. https://doi.org/10.1029/2006JG000313.
Swayze, G.A., Lowers, H.A., Driscoll, R.L., Clark, R.N., 2009. Determining vermiculite source and amphibole content with IR spectroscopy and electron probe microanalysis. In: SME Annual Meeting & Exhibit & CMA 111th National Western Mining Conference, p. 217.
Swayze, G.A., et al., 2018a. Characterizing the source of potentially asbestos-bearing commercial vermiculite insulation using in situ IR spectroscopy. Am. Mineral. 103, 517–549. https://doi.org/10.2138/am-2018-6022.
Swayze, G.A., et al., 2018b. Spectroscopy of expanded vermiculite products and insulation. In: U.S. Geological Survey data release. https://doi.org/10.5066/F7JM27SR.
Ta, K., et al., 2017. Hydrothermal nontronite formation associated with microbes from low-temperature diffuse hydrothermal vents at the South Mid-Atlantic Ridge. JGR Biogeosci. 122, 2375–2392. https://doi.org/10.1002/2017JG003852.
Tanaka, K.L., et al., 2014. Geologic map of Mars. In: U.S.G.S. Geologic Investigations. https://doi.org/10.3133/sim3292.
Thomas, N., et al., 2017. The colour and stereo surface imaging system (CaSSIS) for the ExoMars trace gas orbiter. SSR 212, 1897–1944. https://doi.org/10.1007/s11214-017-0421-1.
Tornabene, L.L., et al., 2017. Image simulation and assessment of the colour and spatial capabilities of the colour and stereo surface imaging system (CaSSIS) on the ExoMars trace gas orbiter. SSR 214, 1–61. https://doi.org/10.1007/s11214-017-0436-7.
Treiman, A.H., et al., 2014. Ferrian saponite from the Santa Monica Mountains (California, USA, earth): characterization as an analog for clay minerals on Mars with application to Yellowknife Bay in Gale Crater. Am. Mineral. 99, 2234–2250. https://doi.org/10.2138/am-2014-4763.
Turner, S.M.R., Fawdon, P., Davis, J.M., 2021. Mineralogy of the Oxia Planum catchment area on Mars and its relevance to the ExoMars Rosalind Franklin rover mission. In: 52nd LPSC Abstracts, p. 2490.
Vago, J.L., et al., 2017. Habitability on Early Mars and the search for biosignatures with the ExoMars rover. Astrobiology 17, 471–510. https://doi.org/10.1089/ast.2016.1533.
Velde, B., 1978. High temperature or metamorphic vermiculites. Cont. Mineral. Petrol. 66, 319–323. https://doi.org/10.1007/BF00373416.
Velde, B., 2010. Origin and Mineralogy of Clays: Clays and the Environment. Springer. ISBN 3642081959.
Viviano-Beck, C.E., et al., 2014. Revised CRISM spectral parameters and summary products based on the currently detected mineral diversity on Mars. JGR Planets 119, 1403–1431. https://doi.org/10.1002/2014JE004627.
Wagner, C., Schade, U., 1996. Measurements and calculations for estimating the spectrometric detection limit for carbonates in Martian soil. Icarus 123, 256–268. https://doi.org/10.1006/icar.1996.0156.
Wilson, W.J., 1970. A study of weathering in a soil derived from a biotite-hornblende rock: !. Weathering of biotite. Clay Miner. 8, 291–303. https://doi.org/10.1180/claymin.1970.008.3.07.
Wray, J.J., et al., 2008. Compositional stratigraphy of clay-bearing layered deposits at Mawrth Vallis, Mars. GRL 35, L12202. https://doi.org/10.1029/2008GL034385.
Wray, J.J., et al., 2009. Diverse aqueous environments on ancient Mars revealed in the southern highlands. Geology 37, 1043–1046. https://doi.org/10.1130/G30331A.1.
Wray, J.J., et al., 2016. Orbital evidence for more widespread carbonate-bearing rocks on Mars. JGR Planets 121, 652–677. https://doi.org/10.1002/2015JE004972.
Zolotov, M.Y., Mironenko, M.V., 2016. Chemical models for Martian weathering profiles: insights into formation of layered phyllosilicate and sulfate deposits. Icarus 275, 203–220. https://doi.org/10.1016/j.icarus.2016.04.011.